Fully coupled photochemistry of the deuterated ionosphere of Mars and its effects on escape of H and D

Eryn Cangi[1], Michael Chaffin[1], Roger Yelle[2], Bethan Gregory[1], Justin Deighan[1]

[1]Laboratory for Atmospheric and Space Physics, University of Colorado Boulder
[2]Lunar and Planetary Laboratory, University of Arizona

Key Points:

- We present the first photochemical modeling study of the deuterated ionosphere of Mars.
- Non-thermal escape dominates D loss under all solar conditions, and the processes producing hot D are similar to those producing hot H.
- The combined D/H fractionation factor is $f = 0.04$–0.07, indicating 147–158 m GEL of water loss, still less than geological estimates.

Corresponding author: Eryn Cangi, eryn.cangi@colorado.edu

Abstract

Although deuterium (D) on Mars has received substantial attention, the deuterated ionosphere remains relatively unstudied. This means that we also know very little about non-thermal D escape from Mars, since it is primarily driven by excess energy imparted to atoms produced in ion-neutral reactions. Most D escape from Mars is expected to be non-thermal, highlighting a gap in our understanding of water loss from Mars. In this work, we set out to fill this knowledge gap. To accomplish our goals, we use an upgraded 1D photochemical model that fully couples ions and neutrals and does not assume photochemical equilibrium. To our knowledge, such a model has not been applied to Mars previously. We model the atmosphere during solar minimum, mean, and maximum, and find that the deuterated ionosphere behaves similarly to the H-bearing ionosphere, but that non-thermal escape on the order of 8000-9000 $cm^{-2}s^{-1}$ dominates atomic D loss under all solar conditions. The total fractionation factor, f, is $f = 0.04$–0.07, and integrated water loss is 147–158 m GEL. This is still less than geomorphological estimates. Deuterated ions at Mars are likely difficult to measure with current techniques due to low densities and mass degeneracies with more abundant H ions. Future missions wishing to measure the deuterated ionosphere in situ will need to develop innovative techniques to do so.

Plain Language Summary

Our knowledge of ions in the martian atmosphere that contain deuterium (D) is extremely limited, lacking measurements and dedicated computer models. This is a problem because the expectation is that most D that escapes to space does so "non-thermally", by gaining extra energy from ion reactions. H and D mostly exist in water on Mars, so identifying how much H and D have escaped non-thermally is an important piece of the puzzle of water loss from Mars. Here, we present the first one dimensional model of the Mars atmosphere that includes D-bearing ions. This new model avoids many common approximations that might change our results in unclear ways. We report the amounts of thermal and non-thermal escape of H and D and confirm that most D escapes non-thermally. We also identify the specific chemical reactions that are most important, and show how many D-bearing ions we expect to find at different altitudes in the atmosphere that might be detectable by future missions. Finally, we calculate that a layer of water 147–158 m deep has been lost from Mars. This is still less than the amount calculated by geological studies.

1 Introduction

Mars is a natural laboratory to study how atmospheric escape shapes planetary habitability. It is now well established that a significant amount of the Mars atmosphere has been lost to space (Jakosky et al., 2018). This escape is fractionating—the relative escape efficiency is different for members of an isotope pair, such as deuterium (D) and hydrogen (H). Because on Mars, D and H are found primarily in water, D/H fractionation indicates a history of water loss (Owen et al., 1988). Understanding escape fractionation therefore contributes to understanding the long-term loss of the atmosphere and desiccation of the planet.

Geological studies indicate that Mars has likely lost 500+ meters global equivalent layer (GEL) of water (Lasue et al., 2013, and references therein), but atmospheric modeling studies typically do not find the same result, instead arriving at a smaller number of 100-250 m GEL (Cangi et al., 2020; Alsaeed & Jakosky, 2019; V. A. Krasnopolsky, 2002; V. Krasnopolsky, 2000). A key step in retrieving water loss estimates from atmospheric models is to quantify both thermal and non-thermal escape.

Thermal escape occurs for particles with a thermal velocity in the high-energy tail of the velocity distribution above the planet's escape velocity. Non-thermal escape comprises

all other processes that grant extra kinetic energy to atmospheric particles, which are variously dubbed "suprathermal" or "hot"; most of these processes involve ion chemistry or interaction with ions. Thermal escape of H has been well-studied at Mars with atmospheric models, observations from missions, and mixes of the two (Chaffin et al., 2021; Stone et al., 2020; Mayyasi et al., 2018; Rahmati et al., 2018; Zahnle et al., 2008; V. A. Krasnopolsky, 2002). Thermal escape of D has also been modeled (Cangi et al., 2020; Kass & Yung, 1999; Yung et al., 1988), but non-thermal escape of D from Mars has not been directly modeled, despite expectations that it should be the dominant loss process (Gacesa et al., 2012; V. A. Krasnopolsky, 2002). V. A. Krasnopolsky (2002) and V. A. Krasnopolsky et al. (1998) calculated non-thermal escape velocities for a few select processes (solar wind charge exchange, electron impact ionization, and photoionization), but their model did not include a deuterated ionosphere, and so missed a portion of the production of hot atoms.

Cangi et al. (2020) used a 1D photochemical model of Mars' neutral atmosphere to calculate the D/H fractionation factor f as a function of atmospheric temperatures. The model only calculated thermal escape directly; non-thermal escape was approximated by scaling the non-thermal effusion velocities given by V. A. Krasnopolsky (2002) and multiplying them by the densities of H and D at the exobase. This estimation indicated that f is several orders of magnitude larger when non-thermal escape processes are considered, motivating a more complete calculation of non-thermal escape of H and D. Here, we present this more complete treatment. The key questions about the deuterated martian ionosphere that we address are as follows.

1. What are the atmospheric densities of deuterated ions?

2. What are the dominant production mechanisms of hot H and hot D, and are they analogous or dissimilar?

3. What is the magnitude of non-thermal escape of D, and is it the dominant type of escape during quiet solar conditions?

4. Can inclusion of non-thermal escape in the model yield an estimation of water loss similar to the amount calculated in geomorphological studies?

To answer these questions, we have upgraded our existing 1D photochemical model of the neutral martian atmosphere to include a self-consistent ionosphere and deuterated ions. Because ions and neutrals have substantially different behaviors and chemistry, the problem of modeling both at the same time turns out to be an expensive and computationally difficult one, even in 1D. Most recent ion-neutral photochemical models use one or more of three common approaches: (1) a fixed (either wholly or partially) background neutral atmosphere (Fox et al., 2021, 2017, 2015; Matta et al., 2013; Molina-Cuberos et al., 2002); (2) placing the lower boundary of the model near the bottom of the ionosphere (Fox et al., 2021; V. A. Krasnopolsky, 2019; Fox et al., 2015; Matta et al., 2013; V. A. Krasnopolsky, 2002); or (3) the assumption of photochemical equilibrium for chemically short-lived species (Vuitton et al., 2019; Banaszkiewicz et al., 2000) and/or neglect of ion diffusion (Dobrijevic et al., 2016). But because we did not want to lose any subtle ion-neutral feedbacks, we have upgraded our photochemical model such that it does not use any of the above simplifcations. In this way, we obtain a more complete understanding of the coupling of the lower to upper atmospheres, which has been recently shown to be key to understanding water transport, destruction, and escape during the Mars dusty season (Villanueva et al., 2021; Chaffin et al., 2021; Holmes et al., 2021; Stone et al., 2020; A. A. Fedorova et al., 2020; Vandaele et al., 2019; Aoki et al., 2019; Heavens et al., 2018).

Our new model spans surface-to-space and fully couples ions and neutrals without assumption of photochemical equilibrium. We use this enhanced model to present a first

theoretical analysis of D ion chemistry at Mars, which includes an updated quantification of non-thermal escape of D and H, the most critical reactions for production of hot H and D, and the implications for water loss.

2 Model description

Here we describe changes made to the 1D photochemical model as described by Cangi et al. (2020). In addition to the upgrades to physics and chemistry described below, this update incorporates computational improvements, such as extensive encapsulation, vectorization of functions, and performance tuning. The only species that we hold constant in our model is argon and lower atmospheric water (see Section 2.1.3). The absolute tolerance is 1 $\times 10^{-12}$, or 1 ppt, and the relative tolerance is 1×10^{-6}.

2.1 New features

2.1.1 Ion reaction network

Our updated model contains ∼600 total ion and neutral reactions. We enumerate the deuterated reactions in Table 1. The full network of chemical reactions is available in the Supporting Information, Table S1; rate coefficients of H-analogue reactions are generally the same as those used by Vuitton et al. (2019).

Scope of deuterated reactions. We define a deuterated analogue reaction as a reaction in which one H atom in one of the reactants has been replaced with D; for example, D + O_2 → DO_2 instead of H + O_2 → HO_2. We do not consider doubly deuterated reactions or species, e.g., we do not include reactions like DO_2 + D → OD + OD nor species like D_2O. Our deuterated reaction network includes the deuterated analogues of the top 23 fastest H-bearing reactions (according to the column rate), including neutral reactions used by (Cangi et al., 2020) and many deuterated analogues of ion-neutral reactions. All told, the H-bearing analogues of these deuterated reactions make up 99.99997% of the integrated column rate of all H-bearing reactions. For this reason, it is unlikely we have missed any significant deuterated reactions.

Table 1: Deuterated reactions used in the model. Reactions 1-6b: column rate ν in $cm^{-2}s^{-1}$. Reactions 7-125: rate coefficients in units of cm^3 $molecule^{-1}$ s^{-1} for bimolecular reactions and cm^6 $molecule^{-1}$ s^{-1} for termolecular reactions. BR = branching ratio; MS = mass scaling.

		Reaction	BR	MS	Rate coefficient	Ref
		Photodissociation and photoionization				
1	D	→ D^+			$\nu_{col} = 0.3$	†
2	DO_2	→ OD + O			$\nu_{col} = 2779$	†
3a	HD	→ HD^+			$\nu_{col} = 0.5$	†
3b		→ H + D			$\nu_{col} = 0.15$	†
3c		→ H^+ + D			$\nu_{col} = 0.03$	†
3d		→ D^+ + H			$\nu_{col} = 0.03$	†
4a	HDO	→ D + OH			$\nu_{col} = 17.4$	C0499
4b		→ H + OD			$\nu_{col} = 17.4$	C0499
4c		→ HD + $O(^1D)$			$\nu_{col} = 2.3$	C0499
4d		→ HDO^+			$\nu_{col} = 1.3$	†
4e		→ OD^+ + H			$\nu_{col} = 0.3$	†
4f		→ OH^+ + D			$\nu_{col} = 0.3$	†
4g		→ D^+ + OH			$\nu_{col} = 0.1$	†
4h		→ H^+ + OD			$\nu_{col} = 0.1$	†

Continued on next page

	Reaction		BR	MS	Rate or rate coefficient	Ref
4i		$\rightarrow O^+ + HD$			$\nu_{col} = 0.02$	†
4j		$\rightarrow H + D + O$			$\nu_{col} = 0$	†
5a	HDO_2	$\rightarrow OH + OD$			$\nu_{col} = 451$	†
5b		$\rightarrow DO_2 + H$			$\nu_{col} = 12.5$	†
5c		$\rightarrow HO_2 + D$			$\nu_{col} = 12.5$	†
5d		$\rightarrow HDO + O(^1D)$			$\nu_{col} = 0$	†
6a	OD	$\rightarrow O + D$			$\nu_{col} = 44.7$	NL84
6b		$\rightarrow O(^1D) + D$			$\nu_{col} = 0.6$	NL84
		Deuterated neutral-neutral reactions				
7	$CO + D$	$\rightarrow DCO$			See text $k_\infty = 1.00e+00 \left(\frac{T_n}{300}\right)^{0.2}$ $k_0 = 2.00 \times 10^{-35} \left(\frac{T_n}{300}\right)^{0.2}$	Est.
8a	$CO + OD$	$\rightarrow CO_2 + D$		$\sqrt{\frac{17}{18}}$	See text $k_\infty = 1.63 \times 10^{-6} \left(\frac{T_n}{300}\right)^{6.1}$ $k_0 = 4.90 \times 10^{-15} \left(\frac{T_n}{300}\right)^{0.6}$	Est.
8b		$\rightarrow DOCO$		$\sqrt{\frac{17}{18}}$	See text $k_\infty = 6.62 \times 10^{-16} \left(\frac{T_n}{300}\right)^{1.3}$ $k_0 = 1.73 \times 10^{-29} \left(\frac{T_n}{300}\right)^{-1.4}$	Est.
9	$D + H_2$	$\rightarrow HD + H$			$2.73 \times 10^{-17} \left(\frac{T_n}{300}\right)^{2.0} e^{-2700/T_n}$	N15
10a	$D + H_2O_2$	$\rightarrow H_2O + OD$	0.5		$1.16 \times 10^{-11} e^{-2110/T_n}$	C10
10b		$\rightarrow HDO + OH$	0.5		$1.16 \times 10^{-11} e^{-2110/T_n}$	C10
11a	$D + HO_2$	$\rightarrow DO_2 + H$			1.00×10^{-10}	Y88
11b		$\rightarrow HD + O_2$			2.45×10^{-12}	Y88
11c		$\rightarrow HDO + O(^1D)$			1.14×10^{-12}	Y88
11d		$\rightarrow OH + OD$			5.11×10^{-11}	Y88
12	$D + O_2$	$\rightarrow DO_2$		$\sqrt{\frac{1}{2}}$	See text $k_\infty = 2.40 \times 10^{-11} \left(\frac{T_n}{300}\right)^{0.2}$ $k_0 = 1.46 \times 10^{-28} \left(\frac{T_n}{300}\right)^{-1.3}$	Est.
13	$D + O_3$	$\rightarrow OD + O_2$			$9.94 \times 10^{-11} e^{-470/T_n}$	Y89, N15
14	$D + OH + CO_2$	$\rightarrow HDO + CO_2$		$\sqrt{\frac{1}{2}}$	$1.16 \times 10^{-25} \left(\frac{T_n}{300}\right)^{-2.0}$	Est.
15	$DCO + H$	$\rightarrow CO + HD$		$\sqrt{\frac{29}{30}}$	1.50×10^{-10}	Est.
16a	$DCO + O$	$\rightarrow CO + OD$		$\sqrt{\frac{29}{30}}$	5.00×10^{-11}	Est.
16b		$\rightarrow CO_2 + D$		$\sqrt{\frac{29}{30}}$	5.00×10^{-11}	Est.
17a	$DCO + O_2$	$\rightarrow CO_2 + OD$		$\sqrt{\frac{29}{30}}$	7.60×10^{-13}	Est.
17b		$\rightarrow DO_2 + CO$		$\sqrt{\frac{29}{30}}$	5.20×10^{-12}	Est.
18	$DCO + OH$	$\rightarrow HDO + CO$	0.5	$\sqrt{\frac{29}{30}}$	1.80×10^{-10}	Est.
19	$DO_2 + HO_2$	$\rightarrow HDO_2 + O_2$		$\sqrt{\frac{33}{34}}$	$3.00 \times 10^{-13} e^{460/T_n}$	Est.
20	$DO_2 + N$	$\rightarrow NO + OD$		$\sqrt{\frac{33}{34}}$	2.20×10^{-11}	Est.
21	$DO_2 + O_3$	$\rightarrow OD + O_2 + O_2$		$\sqrt{\frac{33}{34}}$	$1.00 \times 10^{-14} e^{-490/T_n}$	Est.
22	$DOCO + O_2$	$\rightarrow DO_2 + CO_2$		$\sqrt{\frac{45}{46}}$	2.09×10^{-12}	Est.
23	$DOCO + OH$	$\rightarrow CO_2 + HDO$		$\sqrt{\frac{45}{46}}$	1.03×10^{-11}	Est.

Continued on next page

	Reaction		BR	MS	Rate or rate coefficient	Ref
24	$H + D + M$	$\rightarrow HD + M$		$\sqrt{\frac{1}{2}}$	$6.62 \times 10^{-27} \left(\frac{T_n}{300}\right)^{-2.27}$	Est.
25a	$H + DO_2$	$\rightarrow HD + O_2$		$\sqrt{\frac{33}{34}}$	3.45×10^{-12}	Est.
25b		$\rightarrow HDO + O(^1D)$		$\sqrt{\frac{33}{34}}$	1.60×10^{-12}	Est.
25c		$\rightarrow HO_2 + D$			$1.85 \times 10^{-10} e^{-890/T_n}$	Y88
25d		$\rightarrow OH + OD$		$\sqrt{\frac{33}{34}}$	7.20×10^{-11}	Est.
26	$H + HD$	$\rightarrow H_2 + D$			$1.15 \times 10^{-11} e^{-3041/T_n}$	N15
27a	$H + HDO_2$	$\rightarrow H_2O + OD$	0.5		$1.16 \times 10^{-11} e^{-2110/T_n}$	C10
27b		$\rightarrow HDO + OH$	0.5		$1.16 \times 10^{-11} e^{-2110/T_n}$	C10
28	$H + OD + CO_2$	$\rightarrow HDO + CO_2$		$\sqrt{\frac{17}{18}}$	$1.16 \times 10^{-25} \left(\frac{T_n}{300}\right)^{-2.0}$	Est.
29	$HCO + D$	$\rightarrow CO + HD$		$\sqrt{\frac{1}{2}}$	1.50×10^{-10}	Est.
30	$HCO + OD$	$\rightarrow HDO + CO$	0.5	$\sqrt{\frac{29}{30}}$	1.80×10^{-10}	Est.
31a	$HD + O$	$\rightarrow OD + H$			$1.68 \times 10^{-12} e^{-4400/T_n}$	N15
31b		$\rightarrow OH + D$			$4.40 \times 10^{-12} e^{-4390/T_n}$	N15
32	$HO_2 + DO_2 + M$	$\rightarrow HDO_2 + O_2 + M$		$\sqrt{\frac{33}{34}}$	$4.20 \times 10^{-33} e^{920/T_n}$	Est.
33	$HOCO + OD$	$\rightarrow CO_2 + HDO$		$\sqrt{\frac{17}{18}}$	1.03×10^{-11}	Est.
34	$O + D$	$\rightarrow OD$		$\sqrt{\frac{1}{2}}$	$8.65 \times 10^{-18} \left(\frac{T_n}{300}\right)^{-0.38}$	Est.
35	$O + DO_2$	$\rightarrow OD + O_2$		$\sqrt{\frac{33}{34}}$	$3.00 \times 10^{-11} e^{200/T_n}$	Est.
36a	$O + HDO_2$	$\rightarrow OD + HO_2$	0.5	$\sqrt{\frac{34}{35}}$	$1.40 \times 10^{-12} e^{-2000/T_n}$	Est.
36b		$\rightarrow OH + DO_2$	0.5	$\sqrt{\frac{34}{35}}$	$1.40 \times 10^{-12} e^{-2000/T_n}$	Est.
37	$O + OD$	$\rightarrow O_2 + D$		$\sqrt{\frac{17}{18}}$	$1.80 \times 10^{-11} e^{180/T_n}$	Est.
38a	$O(^1D) + HD$	$\rightarrow D + OH$			4.92×10^{-11}	Y88
38b		$\rightarrow H + OD$			4.92×10^{-11}	Y88
39	$O(^1D) + HDO$	$\rightarrow OD + OH$		$\sqrt{\frac{18}{19}}$	$1.63 \times 10^{-10} e^{60/T_n}$	Est.
40	$OD + H$	$\rightarrow OH + D$			$4.58 \times 10^{-9} \left(\frac{T_n}{300}\right)^{-0.63} e^{-717/T_n}$	Y88
41	$OD + H_2$	$\rightarrow HDO + H$			$2.80 \times 10^{-12} e^{-1800/T_n}$	Y88
42	$OD + H_2O_2$	$\rightarrow HDO + HO_2$		$\sqrt{\frac{17}{18}}$	$2.90 \times 10^{-12} e^{-160/T_n}$	Est.
43	$OD + HO_2$	$\rightarrow HDO + O_2$		$\sqrt{\frac{17}{18}}$	$4.80 \times 10^{-11} e^{250/T_n}$	Est.
44	$OD + O_3$	$\rightarrow DO_2 + O_2$		$\sqrt{\frac{17}{18}}$	$1.70 \times 10^{-12} e^{-940/T_n}$	Est.
45a	$OD + OH$	$\rightarrow HDO + O$		$\sqrt{\frac{17}{18}}$	1.80×10^{-12}	Est.
45b		$\rightarrow HDO_2$		$\sqrt{\frac{17}{18}}$	See text $k_\infty = 2.60 \times 10^{-11}$ $k_0 = 2.69 \times 10^{-28} \left(\frac{T_n}{300}\right)^{-1.0}$	Est.
46	$OH + D$	$\rightarrow OD + H$			$3.30 \times 10^{-9} \left(\frac{T_n}{300}\right)^{-0.63}$	Y88
47	$OH + DO_2$	$\rightarrow HDO + O_2$		$\sqrt{\frac{33}{34}}$	$4.80 \times 10^{-11} e^{250/T_n}$	Est.
48a	$OH + HD$	$\rightarrow H_2O + D$			$4.20 \times 10^{-13} e^{-1800/T_n}$	Y88
48b		$\rightarrow HDO + H$			$5.00 \times 10^{-12} e^{-2130/T_n}$	S11
49a	$OH + HDO_2$	$\rightarrow H_2O + DO_2$	0.5	$\sqrt{\frac{34}{35}}$	$2.90 \times 10^{-12} e^{-160/T_n}$	Est.
49b		$\rightarrow HDO + HO_2$	0.5	$\sqrt{\frac{34}{35}}$	$2.90 \times 10^{-12} e^{-160/T_n}$	Est.
	Deuterated ion-neutral reactions					
50	$ArD^+ + CO$	$\rightarrow DCO^+ + Ar$			1.25×10^{-9}	A03

Continued on next page

	Reaction		BR	MS	Rate or rate coefficient	Ref
51	$ArD^+ + CO_2$	$\rightarrow DCO_2^+ + Ar$			1.10×10^{-9}	A03
52a	$ArD^+ + H_2$	$\rightarrow ArH^+ + HD$			4.50×10^{-10}	A03
52b		$\rightarrow H_2D^+ + Ar$			8.80×10^{-10}	A03
53	$ArD^+ + N_2$	$\rightarrow N_2D^+ + Ar$			6.00×10^{-10}	A03
54	$ArH^+ + HD$	$\rightarrow H_2D^+ + Ar$			8.60×10^{-10}	A03
55a	$Ar^+ + HD$	$\rightarrow ArD^+ + H$			3.84×10^{-10}	A03
55b		$\rightarrow ArH^+ + D$			3.68×10^{-10}	A03
55c		$\rightarrow HD^+ + Ar$			4.80×10^{-11}	A03
56a	$CO_2^+ + D$	$\rightarrow DCO^+ + O$			6.38×10^{-11}	A03
56b		$\rightarrow D^+ + CO_2$			2.02×10^{-11}	A03
57a	$CO_2^+ + HD$	$\rightarrow DCO_2^+ + H$	0.5	$\sqrt{\frac{2}{3}}$	2.35×10^{-10}	Est.
57b		$\rightarrow HCO_2^+ + D$	0.5	$\sqrt{\frac{2}{3}}$	2.35×10^{-10}	Est.
58a	$CO_2^+ + HDO$	$\rightarrow DCO_2^+ + OH$	0.5	$\sqrt{\frac{18}{19}}$	3.00×10^{-10}	Est.
58b		$\rightarrow HCO_2^+ + OD$	0.5	$\sqrt{\frac{18}{19}}$	3.00×10^{-10}	Est.
58c		$\rightarrow HDO^+ + CO_2$		$\sqrt{\frac{18}{19}}$	1.80×10^{-9}	Est.
59	$CO^+ + D$	$\rightarrow D^+ + CO$			9.00×10^{-11}	A03
60a	$CO^+ + HD$	$\rightarrow DCO^+ + H$	0.25	$\sqrt{\frac{2}{3}}$	7.50×10^{-10}	Est.
60b		$\rightarrow DOC^+ + H$	0.25	$\sqrt{\frac{2}{3}}$	7.50×10^{-10}	Est.
60c		$\rightarrow HCO^+ + D$	0.25	$\sqrt{\frac{2}{3}}$	7.50×10^{-10}	Est.
60d		$\rightarrow HOC^+ + D$	0.25	$\sqrt{\frac{2}{3}}$	7.50×10^{-10}	Est.
61a	$CO^+ + HDO$	$\rightarrow DCO^+ + OH$	0.5	$\sqrt{\frac{18}{19}}$	8.40×10^{-10}	Est.
61b		$\rightarrow HCO^+ + OD$	0.5	$\sqrt{\frac{18}{19}}$	8.40×10^{-10}	Est.
61c		$\rightarrow HDO^+ + CO$		$\sqrt{\frac{18}{19}}$	1.56×10^{-9}	Est.
62	$C^+ + HD$	$\rightarrow CH^+ + D$	0.17		1.20×10^{-16}	A03
63a	$C^+ + HDO$	$\rightarrow DCO^+ + H$	0.5	$\sqrt{\frac{18}{19}}$	$7.80 \times 10^{-9} \left(\frac{T_i}{300}\right)^{-0.5}$	Est.
63b		$\rightarrow DOC^+ + H$	0.5	$\sqrt{\frac{18}{19}}$	1.08×10^{-9}	Est.
63c		$\rightarrow HCO^+ + D$	0.5	$\sqrt{\frac{18}{19}}$	$7.80 \times 10^{-9} \left(\frac{T_i}{300}\right)^{-0.5}$	Est.
63d		$\rightarrow HDO^+ + C$			2.34×10^{-10}	Est.
63e		$\rightarrow HOC^+ + D$	0.5	$\sqrt{\frac{18}{19}}$	1.08×10^{-9}	Est.
64	$DCO_2^+ + CO$	$\rightarrow DCO^+ + CO_2$		$\sqrt{\frac{45}{46}}$	7.80×10^{-10}	Est.
65a	$DCO_2^+ + e^-$	$\rightarrow CO + O$	0.68		$4.62 \times 10^{-5} \left(\frac{T_i}{300}\right)^{-0.64}$	G05
65b		$\rightarrow CO + OD$	0.27		$4.62 \times 10^{-5} \left(\frac{T_i}{300}\right)^{-0.64}$	G05
65c		$\rightarrow CO_2 + D$	0.05		$4.62 \times 10^{-5} \left(\frac{T_i}{300}\right)^{-0.64}$	G05
66	$DCO_2^+ + H_2O$	$\rightarrow H_2DO^+ + CO_2$		$\sqrt{\frac{45}{46}}$	2.65×10^{-9}	Est.
67	$DCO_2^+ + O$	$\rightarrow DCO^+ + O_2$		$\sqrt{\frac{45}{46}}$	5.80×10^{-10}	Est.
68a	$DCO^+ + e^-$	$\rightarrow CO + D$	0.92		$9.02 \times 10^{-5} \left(\frac{T_i}{300}\right)^{-1.1}$	GK
68b		$\rightarrow OD + C$	0.07		$9.02 \times 10^{-5} \left(\frac{T_i}{300}\right)^{-1.1}$	GK
69	$DCO^+ + H$	$\rightarrow HCO^+ + D$			1.50×10^{-11}	A03
70	$DCO^+ + H_2O$	$\rightarrow H_2DO^+ + CO$		$\sqrt{\frac{29}{30}}$	2.60×10^{-9}	Est.
71	$DOC^+ + CO$	$\rightarrow DCO^+ + CO$		$\sqrt{\frac{29}{30}}$	6.00×10^{-10}	Est.

Continued on next page

	Reaction		BR	MS	Rate or rate coefficient	Ref
72	$DOC^+ + e^-$	$\rightarrow OD + C$		$\sqrt{\frac{29}{30}}$	$1.19 \times 10^{-8} \left(\frac{T_i}{300}\right)^{1.2}$	Est.
73a	$DOC^+ + H_2$	$\rightarrow H_2D^+ + CO$	0.57		6.20×10^{-10}	A03
73b		$\rightarrow HCO^+ + HD$	0.43		6.20×10^{-10}	A03
74a	$D^+ + CO_2$	$\rightarrow CO_2^+ + D$			3.50×10^{-9}	A03
74b		$\rightarrow DCO^+ + O$			2.60×10^{-9}	A03
75	$D^+ + H$	$\rightarrow D + H^+$	0.87		$6.50 \times 10^{-11} \left(\frac{T_i}{300}\right)^{0.5}$	Y89
76	$D^+ + H_2$	$\rightarrow H^+ + HD$			2.20×10^{-9}	A03
77a	$D^+ + H_2O$	$\rightarrow H_2O^+ + D$			5.20×10^{-9}	A03
77b		$\rightarrow HDO^+ + H$	0.5	$\sqrt{\frac{1}{2}}$	8.20×10^{-9}	Est.
78	$D^+ + NO$	$\rightarrow NO^+ + D$			1.80×10^{-9}	A03
79	$D^+ + O$	$\rightarrow D + O^+$			2.80×10^{-10}	A03
80	$D^+ + O_2$	$\rightarrow O_2^+ + D$			1.60×10^{-9}	A03
81a	$H_2DO^+ + e^-$	$\rightarrow H_2 + O$	0.5	$\sqrt{\frac{19}{20}}$	$9.68 \times 10^{-8} \left(\frac{T_i}{300}\right)^{-0.5}$	Est.
81b		$\rightarrow H_2O + D$	0.5	$\sqrt{\frac{19}{20}}$	$1.86 \times 10^{-6} \left(\frac{T_i}{300}\right)^{-0.5}$	Est.
81c		$\rightarrow HD + O$	0.5	$\sqrt{\frac{19}{20}}$	$9.68 \times 10^{-8} \left(\frac{T_i}{300}\right)^{-0.5}$	Est.
81d		$\rightarrow HDO + H$	0.5	$\sqrt{\frac{19}{20}}$	$1.86 \times 10^{-6} \left(\frac{T_i}{300}\right)^{-0.5}$	Est.
81e		$\rightarrow OD + H$	0.5	$\sqrt{\frac{19}{20}}$	$4.47 \times 10^{-6} \left(\frac{T_i}{300}\right)^{-0.5}$	Est.
81f		$\rightarrow OD + H_2$	0.5	$\sqrt{\frac{19}{20}}$	$1.04 \times 10^{-6} \left(\frac{T_i}{300}\right)^{-0.5}$	Est.
81g		$\rightarrow OH + D$	0.5	$\sqrt{\frac{19}{20}}$	$4.47 \times 10^{-6} \left(\frac{T_i}{300}\right)^{-0.5}$	Est.
81h		$\rightarrow OH + HD$	0.5	$\sqrt{\frac{19}{20}}$	$1.04 \times 10^{-6} \left(\frac{T_i}{300}\right)^{-0.5}$	Est.
82a	$H_2D^+ + CO$	$\rightarrow DCO^+ + H_2$	0.33		1.60×10^{-9}	A03
82b		$\rightarrow HCO^+ + HD$	0.67		1.60×10^{-9}	A03
83	$H_2D^+ + H_2$	$\rightarrow H_3^+ + HD$			5.30×10^{-10}	A03
84a	$H_2O^+ + HD$	$\rightarrow H_2DO^+ + H$	0.5	$\sqrt{\frac{2}{3}}$	3.80×10^{-10}	Est.
84b		$\rightarrow H_3O^+ + D$	0.5	$\sqrt{\frac{2}{3}}$	3.80×10^{-10}	Est.
85	$HCO_2^+ + HDO$	$\rightarrow H_2DO^+ + CO_2$		$\sqrt{\frac{18}{19}}$	2.65×10^{-9}	Est.
86	$HCO^+ + D$	$\rightarrow DCO^+ + H$			4.25×10^{-11}	A03
87	$HCO^+ + HDO$	$\rightarrow H_2DO^+ + CO$		$\sqrt{\frac{18}{19}}$	2.60×10^{-9}	Est.
88a	$HDO^+ + CO$	$\rightarrow DCO^+ + OH$	0.5	$\sqrt{\frac{18}{19}}$	2.12×10^{-10}	Est.
88b		$\rightarrow HCO^+ + OD$	0.5	$\sqrt{\frac{18}{19}}$	2.12×10^{-10}	Est.
89a	$HDO^+ + e^-$	$\rightarrow HD + O$		$\sqrt{\frac{18}{19}}$	$2.64 \times 10^{-6} \left(\frac{T_i}{300}\right)^{-0.74}$	Est.
89b		$\rightarrow O + D$		$\sqrt{\frac{18}{19}}$	$2.08 \times 10^{-5} \left(\frac{T_i}{300}\right)^{-0.74}$	Est.
89c		$\rightarrow OD + H$	0.5	$\sqrt{\frac{18}{19}}$	$5.86 \times 10^{-6} \left(\frac{T_i}{300}\right)^{-0.74}$	Est.
89d		$\rightarrow OH + D$	0.5	$\sqrt{\frac{18}{19}}$	$5.86 \times 10^{-6} \left(\frac{T_i}{300}\right)^{-0.74}$	Est.
90a	$HDO^+ + H_2$	$\rightarrow H_2DO^+ + H$	0.5	$\sqrt{\frac{18}{19}}$	3.80×10^{-10}	Est.
90b		$\rightarrow H_3O^+ + D$	0.5	$\sqrt{\frac{18}{19}}$	3.80×10^{-10}	Est.
91a	$HDO^+ + N$	$\rightarrow HNO^+ + D$	0.5	$\sqrt{\frac{18}{19}}$	5.60×10^{-11}	Est.
91b		$\rightarrow NO^+ + HD$		$\sqrt{\frac{18}{19}}$	2.80×10^{-11}	Est.
92	$HDO^+ + NO$	$\rightarrow NO^+ + HDO$		$\sqrt{\frac{18}{19}}$	4.60×10^{-10}	Est.

Continued on next page

	Reaction		BR	MS	Rate or rate coefficient	Ref
93	$HDO^+ + O$	$\rightarrow O_2^+ + HD$		$\sqrt{\frac{18}{19}}$	4.00×10^{-11}	Est.
94	$HDO^+ + O_2$	$\rightarrow O_2^+ + HDO$		$\sqrt{\frac{18}{19}}$	3.30×10^{-10}	Est.
95a	$HD^+ + Ar$	$\rightarrow ArD^+ + H$	0.45	$\sqrt{\frac{2}{3}}$	2.10×10^{-9}	A03
95b		$\rightarrow ArH^+ + D$	0.55	$\sqrt{\frac{2}{3}}$	2.10×10^{-9}	Est.
96a	$HD^+ + CO$	$\rightarrow DCO^+ + H$	0.5	$\sqrt{\frac{2}{3}}$	1.45×10^{-9}	Est.
96b		$\rightarrow HCO^+ + D$	0.5	$\sqrt{\frac{2}{3}}$	1.45×10^{-9}	Est.
97a	$HD^+ + CO_2$	$\rightarrow DCO_2^+ + H$	0.5	$\sqrt{\frac{2}{3}}$	1.17×10^{-9}	Est.
97b		$\rightarrow HCO_2^+ + D$	0.5	$\sqrt{\frac{2}{3}}$	1.17×10^{-9}	Est.
98	$HD^+ + e^-$	$\rightarrow H + D$			$1.93 \times 10^{-6} \left(\frac{T_i}{300}\right)^{-0.853} e^{-43.3/T_i}$	K19
99	$HD^+ + HD$	$\rightarrow H_2D^+ + D$			8.42×10^{-10}	A03
100a	$HD^+ + N_2$	$\rightarrow N_2D^+ + H$	0.5	$\sqrt{\frac{2}{3}}$	1.00×10^{-9}	Est.
100b		$\rightarrow N_2H^+ + D$	0.5	$\sqrt{\frac{2}{3}}$	1.00×10^{-9}	Est.
101a	$HD^+ + O$	$\rightarrow OD^+ + H$	0.5	$\sqrt{\frac{2}{3}}$	7.50×10^{-10}	Est.
101b		$\rightarrow OH^+ + D$	0.5	$\sqrt{\frac{2}{3}}$	7.50×10^{-10}	Est.
102	$HD^+ + O_2$	$\rightarrow HO_2^+ + D$	0.5	$\sqrt{\frac{2}{3}}$	9.60×10^{-10}	Est.
103	$H^+ + HD$	$\rightarrow D^+ + H_2$			1.10×10^{-10}	A03
104a	$H^+ + HDO$	$\rightarrow H_2O^+ + D$	0.5	$\sqrt{\frac{18}{19}}$	8.20×10^{-9}	Est.
104b		$\rightarrow HDO^+ + H$	0.5	$\sqrt{\frac{18}{19}}$	8.20×10^{-9}	Est.
105	$N_2D^+ + CO$	$\rightarrow DCO^+ + N_2$		$\sqrt{\frac{29}{30}}$	8.80×10^{-10}	Est.
106	$N_2D^+ + e^-$	$\rightarrow N_2 + D$		$\sqrt{\frac{29}{30}}$	$6.60 \times 10^{-7} \left(\frac{T_i}{300}\right)^{-0.51}$	Est.
107	$N_2D^+ + H$	$\rightarrow N_2H^+ + D$			2.50×10^{-11}	A03
108	$N_2D^+ + O$	$\rightarrow OD^+ + N_2$		$\sqrt{\frac{29}{30}}$	1.40×10^{-10}	Est.
109	$N_2H^+ + D$	$\rightarrow N_2D^+ + H$			8.00×10^{-11}	A03
110	$N_2^+ + D$	$\rightarrow D^+ + N_2$			1.20×10^{-10}	A03
111a	$N_2^+ + HD$	$\rightarrow N_2D^+ + H$	0.51		1.34×10^{-9}	A03
111b		$\rightarrow N_2H^+ + D$	0.49		1.34×10^{-9}	A03
112a	$N_2^+ + HDO$	$\rightarrow HDO^+ + N_2$		$\sqrt{\frac{18}{19}}$	1.90×10^{-9}	Est.
112b		$\rightarrow N_2D^+ + OH$	0.5	$\sqrt{\frac{18}{19}}$	5.04×10^{-10}	Est.
112c		$\rightarrow N_2H^+ + OD$	0.5	$\sqrt{\frac{18}{19}}$	5.04×10^{-10}	Est.
113	$N^+ + HD$	$\rightarrow NH^+ + D$	0.25		3.10×10^{-10}	A03
114	$OD^+ + CO$	$\rightarrow DCO^+ + O$		$\sqrt{\frac{17}{18}}$	8.40×10^{-10}	Est.
115	$OD^+ + CO_2$	$\rightarrow DCO_2^+ + O$		$\sqrt{\frac{17}{18}}$	1.35×10^{-9}	Est.
116	$OD^+ + e^-$	$\rightarrow O + D$		$\sqrt{\frac{17}{18}}$	$6.50 \times 10^{-7} \left(\frac{T_i}{300}\right)^{-0.5}$	Est.
117a	$OD^+ + H_2$	$\rightarrow H_2O^+ + D$	0.5	$\sqrt{\frac{17}{18}}$	9.70×10^{-10}	Est.
117b		$\rightarrow HDO^+ + H$	0.5	$\sqrt{\frac{17}{18}}$	9.70×10^{-10}	Est.
118	$OD^+ + N$	$\rightarrow NO^+ + D$		$\sqrt{\frac{17}{18}}$	8.90×10^{-10}	Est.
119	$OD^+ + N_2$	$\rightarrow N_2D^+ + O$		$\sqrt{\frac{17}{18}}$	2.40×10^{-10}	Est.
120	$OD^+ + O$	$\rightarrow O_2^+ + D$		$\sqrt{\frac{17}{18}}$	7.10×10^{-10}	Est.
121	$OD^+ + O_2$	$\rightarrow O_2^+ + OD$		$\sqrt{\frac{17}{18}}$	3.80×10^{-10}	Est.

Continued on next page

	Reaction		BR	MS	Rate or rate coefficient	Ref
122a	$OH^+ + HD$	$\rightarrow H_2O^+ + D$		$\sqrt{\frac{2}{3}}$	9.70×10^{-10}	Est.
122b		$\rightarrow HDO^+ + H$		$\sqrt{\frac{2}{3}}$	9.70×10^{-10}	Est.
123	$O^+ + D$	$\rightarrow D^+ + O$		$\sqrt{\frac{1}{2}}$	6.40×10^{-10}	Est.
124a	$O^+ + HD$	$\rightarrow OD^+ + H$	0.46		1.25×10^{-9}	A03
124b		$\rightarrow OH^+ + D$	0.54		1.25×10^{-9}	A03
125	$O^+ + HDO$	$\rightarrow HDO^+ + O$		$\sqrt{\frac{18}{19}}$	2.60×10^{-9}	Est.

NL84: Nee and Lee (1984). Y88: Anicich (2003). Y89: Yung et al. (1989). A03: Anicich (2003). C0499: Cheng et al. (2004); Cheng et al. (1999). G05: Geppert et al. (2005). K09: Korolov et al. (2009). GK: Rate from K09, branching ratio from G05. C10: Cazaux et al. (2010). S11: Sander et al. (2011). N: Manion et al. (2015). K19: Wakelam and Gratier (2019). Est: Estimated with mass scaling. †: Assumed same as H-analogue.

Photodissociation and photoionization: Photodissociation and ionization of deuterated species is calculated using the solar spectrum (see Section 2.2.2), so the entry in the table under 'Rate or rate coefficient' represents the integrated column rate. The 'Ref' column refers to the source of the cross sections used. For photoionization cross sections of the H-analogue reactions, see Vuitton et al. (2019, and references therein).

Neutral and ion bimolecular and termolecular reactions: The rate coefficient used for a given reaction is the product of the 'BR', 'MS' and 'Rate coefficient' columns (empty fields are taken to be 1). 'BR', or branching ratio, accounts for the fact that deuteration of a reaction can create two or more branches with differing products where only one branch would exist for the H-analogue reaction. 'MS', or mass scaling, is a scaling factor equal to the square root of the mass ratio, $\sqrt{m_1/m_2}$, where m_2 is the mass of the deuterated species and m_1 the H-bearing species. This factor is applied to reactions for which we were not able to find a measurement in the literature to account for replacement of one reactant H atom with one D atom; a similar approach was used previously by V. A. Krasnopolsky (2002) for reactions of neutral HD with dominant ions and minor H-bearing ions.

Most reactions in these tables proceed using the listed rate coefficients. A few exceptions apply; the categorization Types and formulae mentioned below are the same as used by Vuitton et al. (2019). A more complete description of the formulae used can be found in their Appendix B.

Reaction 7: Similar to its analogue CO + H → HCO, this is a Type 4 (pressure dependent association) reaction. The Troe parameter for this reaction is 0, so we use the form:

$$k = k_R + \frac{(Mk_0k_\infty)}{Mk_0 + k_\infty} \tag{1}$$

Where k_R is 0 in this case and M is the background atmospheric density.

Reactions 8a, 8b, 12, and 45b: These are Type 6 (CO + OD → CO_2 + D) and Type 5 (CO + OH → DOCO, D + O_2→ DO_2, OD + OH → HDO_2) pressure dependent bimolecular reactions, with the formulae originally given by Burkholder et al. (2019); Sander et al. (2011). We use the same forms here, but multiplied by our mass scaling factor.

Ion reactions which produce a lone D or H atom have the potential to cause the produced atom to be "hot", that is, gaining enough excess energy from the reaction that they can escape. We describe this in more detail in Section 2.1.4.

2.1.2 Ambipolar diffusion

The model employs ambipolar diffusion for all ions, using the Langevin-Gioumousis-Stevenson equation (Bauer, 1973):

$$D_{ai} = \frac{k(T_i + T_e)}{m_i \sum \nu_{ij}} \tag{2}$$

$$\nu_{ij} = 2\pi \left(\frac{\alpha_j e^2}{\mu_{ij}} \right)^{1/2} n_j \tag{3}$$

Where D_{ai} is the ambipolar diffusion coefficient for ion i, ν_{ij} is the collision frequency of ion i with neutral j, α_j is the polarizability, e is the fundamental charge, and n is the neutral density. Polarizability values for neutrals are collected from Manion et al. (2015). Where polarizability was not available either in data or models for a deuterated species we include, we assumed the same value as the H-bearing analogue.

2.1.3 Partially fixed water profile

We assume a constant abundance of water in the lower atmosphere, which approximates the average water available due to seasonal cycles of polar cap sublimation and transport. The mixing ratio is 1.3 $\times 10^{-4}$ up to the hygropause (which we take to be 40 km, between 25 km by V. A. Krasnopolsky (2002) and its enhanced altitude of 50-80 km during dust storms (Heavens et al., 2018)). The hygropause on Mars represents the altitude at which water begins to condense; in our model, which does not include microphysics or phase changes, the hygropause altitude is the point at which the water mixing ratio begins to follows the saturation vapor pressure curve. At 72 km, a minimum of saturation is reached; above that level, the abundance of water is a free variable. This allows a more holistic understanding of water and water ion chemistry in the upper atmosphere, which has been shown to be an important tracer of seasonal H escape (Stone et al., 2020). The total amount of water in the atmosphere is 10.5 pr μm, in accordance with observations (Smith, 2004; Lammer et al., 2003).

2.1.4 Non-thermal escape

Although there are many non-thermal escape mechanisms, in this work, we focus on photochemical loss, i.e. the contribution to escape from chemistry and photochemistry. We neglect processes involving the solar wind such as sputtering, ion pickup, and charge exchange with the solar wind. Processes which depend upon the solar wind will primarily occur above the bow shock (which is far above our top boundary), where the solar wind can interact with the corona before being mostly deflected around the planet (Halekas et al., 2017). By focusing on planetary ionospheric reactions, we capture the non-thermal escape of H and D sourced from the atmosphere below the exobase.

We calculate the non-thermal escape of hot atoms created via ion-neutral chemistry as the product of the probability of escape and the volume production rate of hot atoms using the procedure described by Gregory et al. (2022). We have evaluated all ion-neutral reactions that produce H, D, H_2, or HD in the model for their exothermicity (following Fox (2015)) and only use those where the excess energy exceeds the escape velocity energy. In reality, the excess heat produced can be split between the two products according to conservation of energy. Information about these heat branching ratios is sparse, even for H species; for this reason, we assume that all excess energy produced ends up in the atomic H or D (see the Supporting Information). We use the escape probability curve calculated by Gregory et al. (2022) for a particle of excess energy 5 eV; this is a reasonable approximation of the actual mean excess energy in our model, with is 3.6 eV.

The resulting volume escape rate can be integrated to obtain an escape flux for the top boundary of the model. Although our focus is escape of atomic H and D, some loss does occur via loss of the molecular form, so we also include non-thermal escape of H_2 and HD. In these cases, we assume that σ_{H_2} is the same as for D due to the similar masses, and that σ_{HD} is larger than H_2 by the same amount that D is larger than H.

2.2 Model inputs

Because the importance of non-thermal escape is expected to vary with solar activity, we have constructed three sets of inputs representing solar minimum, mean, and maximum conditions. The only properties which we vary between these cases are the neutral exobase temperatures and the incoming solar flux. Figure 1 shows these inputs in the navy, purple, and yellow colors. The inputs represent a dayside mean atmosphere (solar zenith angle [SZA]=60°).

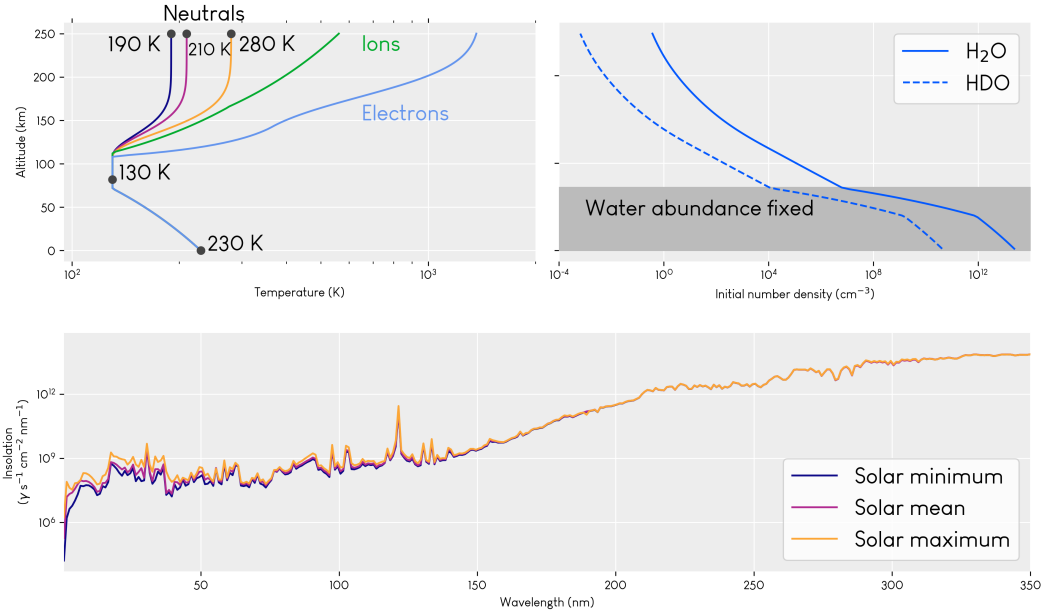

Figure 1. Main model inputs. a) Temperature profiles, with separate neutral exobase temperatures for each solar condition. Ion and electron temperatures are fits to data from MAVEN/STATIC as reported by Hanley et al. (2022) and MAVEN/LPW as reported by Ergun et al. (2015). b) Initial water profile. Above 72 km, water densities evolve according to the chemistry and transport. c) Insolation profiles from 0-300 nm for solar minimum, mean, and maximum. The full input spectrum goes out to 2400 nm, but the insolation there is relatively flat, with no variation due to solar cycle.

2.2.1 Atmospheric temperature profiles

Standard neutral temperatures were obtained from the Mars Climate Database (Millour & Forget, 2018) by several layers of averaging, in order of first to last: by longitude, local time (9, 12, and 3 pm local times, night excluded), latitude (weighted by encompassed surface area), and L_s. Over the solar cycle, the only significant change is to the exobase temperature, so we hold the surface and mesospheric temperature constant at 230 K and 130 K respectively.

In order to support modeling of ion chemistry, we use a piecewise fit to the new ion temperature profiles obtained at SZA=60° with the STATIC instrument by Hanley et al. (2022). These new data have overturned long-standing assumptions that the neutrals, ions, and

electrons thermalize to the same temperature around 125 km (Schunk & Nagy, 2009), and thus represent a significant update in Mars photochemistry. We also include a fit to the electron profile from MAVEN/LPW (Ergun et al., 2015). Because it is difficult to associate ion temperatures with contemporary neutral temperatures due to the averaging required for the neutral profiles, and because the data are limited in time, we do not change the ion or electron profiles for the different solar cycle scenarios, although in the real atmosphere, enhanced solar activity would likely lead to enhanced ion and electron temperatures.

2.2.2 Insolation

Incoming solar photons are key reactants in photochemical reactions. For each solar case, we include photon fluxes from 0.5–2400 nm, binned in 1 nm increments. Total flux, once obtained, is scaled to Mars' orbit and SZA=60°.

We determined the dates of recent representative solar conditions by looking for periods when Ly α irradiance in the Lyman-alpha Model Solar Spectral Irradiance data set (Woods et al., 2019) reached a peak, average, or trough. Because solar maximum and mean in recent decades have been historically quiet, we chose dates from the early 2000s to get a more representative photon flux for maximum and mean (solar minimum has not changed much). The dates we used were February 25, 2019 for solar minimum; February 7, 2004 for mean; and March 22, 2002 for maximum.

For the insolation flux data, we use SORCE/SOLSTICE at solar minimum and mean, and a mix of SORCE/SOLSTICE and TIMED/SEE at solar maximum. There is an additional complication for solar maximum: SORCE/SOLSTICE began a year after our solar maximum date, but includes the longer wavelengths we need, while TIMED/SEE began before our solar maximum date, but only includes fluxes at wavelengths shortwards of 190 nm. We patched together these two datasets, using SORCE/SOLSTICE for wavelengths 190-2000 nm from June 4, 2015 and TIMED/SEE for wavelengths 0.5-189.5 nm from March 22, 2002.

Figure 1a shows the fluxes only from 0.5 to 300 nm for simplicity; longwards of 300 nm, the profile does not vary over the solar cycle. The region shortward of 300 nm is also more important for photochemistry as the photodissociation and photoionization cross sections are largest there. We use the same cross sections as Cangi et al. (2020), with the addition of new photoionization and a few neutral photodissociation cross sections, the same used by Vuitton et al. (2019).

2.3 Boundary conditions

We use mostly the same boundary conditions as Cangi et al. (2020). The key addition is an additional non-thermal flux boundary condition at the top of the model for H, D, H_2, and HD, according to the functional form described by (Gregory et al., 2022). Flux is zero at the top and bottom of the model for all ion species and any neutral species without a different boundary condition.

It is worth emphasizing that our flux boundary condition at the top of the model for atomic O is fixed at $1.2{\times}10^8$ cm^{-2}s^{-1}. Over long simulation times where the atmosphere reaches equilibrium, the sum $\phi_{\mathrm{H}} + \phi_{\mathrm{D}}$ will naturally evolve to equal twice the O escape flux, since H_2O and HDO are the primary source of H and D in the model. This is a feature of the atmosphere in long-term equilibrium, but it does not necessarily occur over shorter timescales– either on the real Mars or in the model.

3 Results

3.1 What are the atmospheric densities of deuterated ions?

The general distribution of the deuterated ionospheric species is similar to that of their H-analogues. Vertical profiles for select species containing H or D are shown in Figure 2. Although they are calculated from surface to 250 km, the figure's lower boundary is

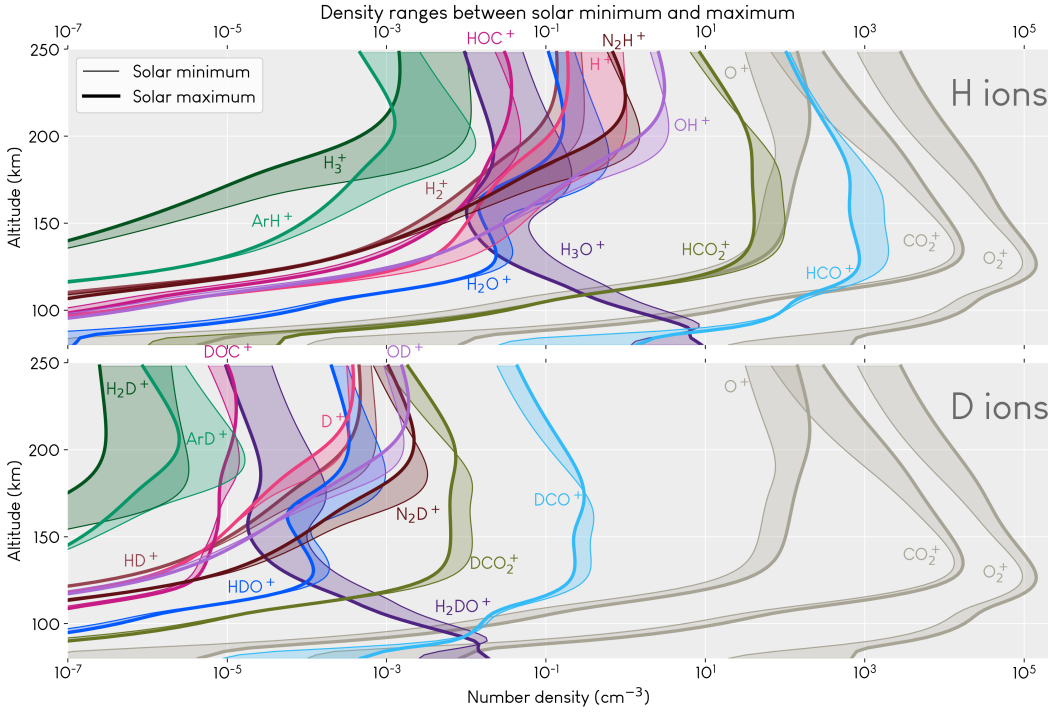

Figure 2. Densities of a) H-bearing ions and b) D-bearing (deuterated). Density ranges are bounded by their values at solar minimum (thin line) and solar maximum (thick line). Gray lines show the primary ionospheric species for comparison. For most species and at most altitudes, densities at solar mean fall within these ranges.

placed at 80 km for legibility. The full image from surface to 250 km showing all species in the model appears in the Supporting Information (Figure S1).

Primary peaks in the densities of deuterated ions occur between 150 and 200 km, with a minor peak near the top of the mesosphere, around 90-125 km. This structure does not hold for all species. H_3O^+ has its peak much lower down at about 90 km, which is in agreement with previous modeling (Fox et al., 2015; Molina-Cuberos et al., 2002). Unfortunately, comparisons with data are not feasible at this altitude because such data do not exist. Most ionic species, H- and D-bearing alike, also display a slight dip in density around 150 km, which is caused by a feature of the same shape in the electron temperature profile (see Figure 1a).

At solar maximum, greater insolation at short wavelengths enables more photoionization, increasing the abundances of primary species CO_2^+, O_2^+, and O^+which are produced directly from the parent neutrals. But for the lighter (and often more minor) ions containing H and D, chemistry and/or transport is a more important driver than photoionization. Temperature-driven changes in the parent neutral densities propagate through to their ions; for example, H^+ abundance at the top of the atmosphere decreases as the temperature goes up because H escape is diffusion-limited, whereas the same is not true for D abundance (Cangi et al., 2020; Zahnle et al., 2008). For other minor species that are not diffusion-limited, higher temperatures can also stimulate faster chemical reactions, slightly enhancing production and therefore density at higher temperatures.

3.1.1 Comparisons with previous works

Here, we compare our results to modeling results by Fox et al. (2015, 2021) and measurements by MAVEN NGIMS (Benna et al., 2015; Fox et al., 2021). In this work, we have parameterized our atmosphere in order to obtain an understanding of the mean-field behavior in time and space. We have not attempted to match the same the modeling input or the relevant atmospheric conditions of those studies. Our models differ substantially from those by Fox et al. (2021, 2015) in temperature structure, boundary conditions (especially for ions at the upper boundary), vertical extent, use of photochemical equilibrium, background atmosphere, SZA, included species, mean Mars-Sun distance, assumed eddy diffusion profile, and included processes (we do not model electron impact ionization or dissociation). Because of these differences, we provide these comparisons primarily for the reader's orientation.

Fox et al. (2015). For the major ions such as O^+, CO_2^+, and O_2^+, our density profiles are generally consistent with those modeled by Fox et al. (2015), as shown in Figure 3. They are also broadly similar for many of the minor ions, although in general, our profiles tend to show lower densities near 250 km by 1-2 orders of magnitude. There is a significant difference between our H_2O^+, H_3O^+, and NO^+ profiles; of these, NO^+ has the largest density overall. It should be noted that many of the ions for which we show a significantly different profile are quite minor, with populations never exceeding 100 cm^{-3}, so the absolute differences as a percent of the total atmosphere are tiny, well within the absolute tolerance. Fox et al. (2015) make the point that their model calculates neutral H_2O produced only by ion-neutral reactions due to their choice of boundary conditions, whereas ours includes production by photodissociation; it is then perhaps not surprising that our results include more water than theirs (see Figure 3d).

In Figure S3, we also compare our results to Fox et al. (2021), which uses a similar model to Fox et al. (2015) and includes recent data from NGIMS for CO_2^+, $O_2^+$and O^+. Compared to that paper, our results are more dissimilar.

Benna et al. (2015), using MAVEN NGIMS. Our results show reasonably good agreement with the initial NGIMS measurements at Mars (Benna et al., 2015) (Figure 4), which occurred long enough into the mission that solar mean conditions would have prevailed. There continues to be a divergence between model and data for O^+in the up-

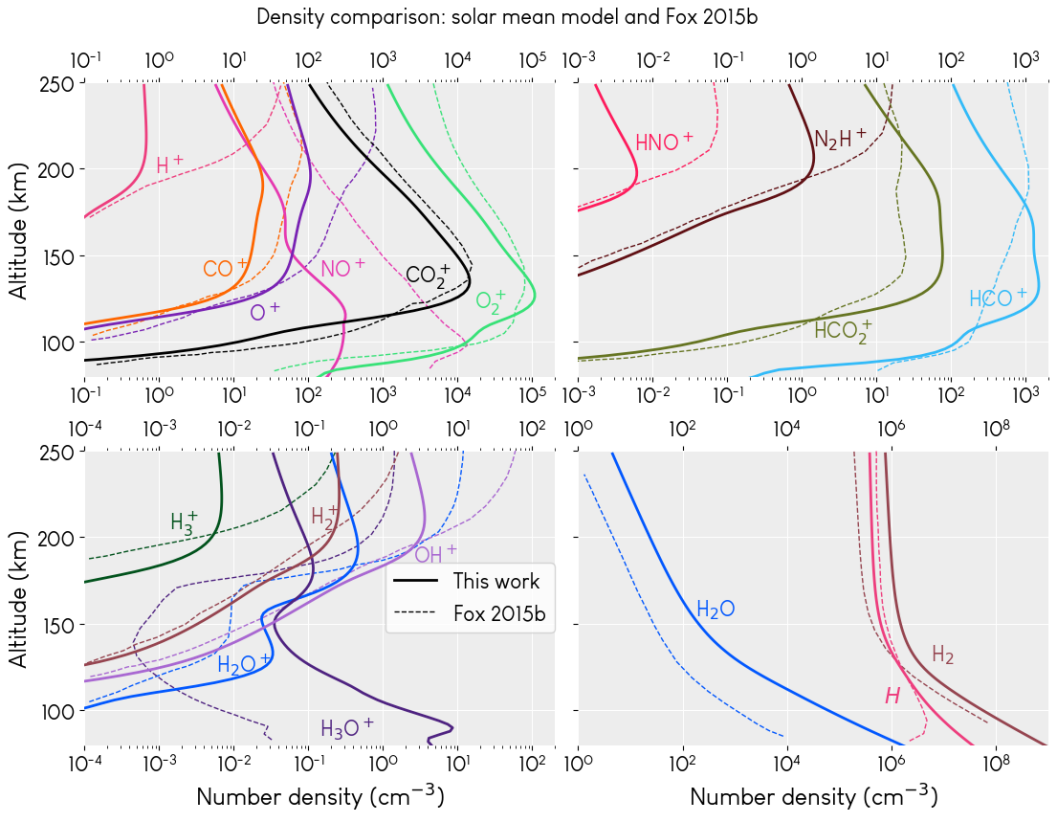

Figure 3. Ion and neutral densities computed by our model and compared with those computed by Fox et al. (2015). Species are divided amongst the four panels for legibility and compared with Figure 3 in Fox et al. (2015). Some minor species are omitted for clarity.

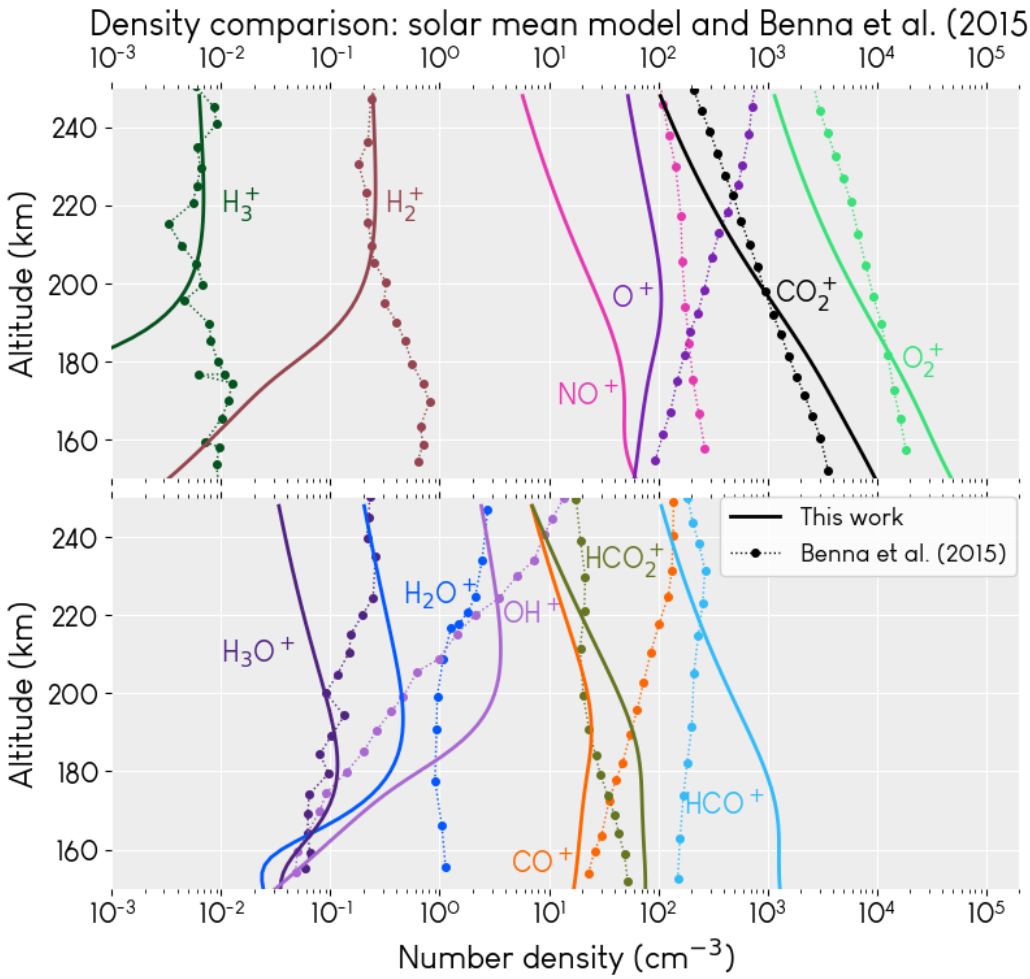

Figure 4. Ion and neutral densities computed by our model and compared with those computed by Benna et al. (2015). Species are divided amongst the two panels for legibility. HNO^+differs significantly from data and has been omitted; the measurements are known to be unreliable due to spacecraft potential.

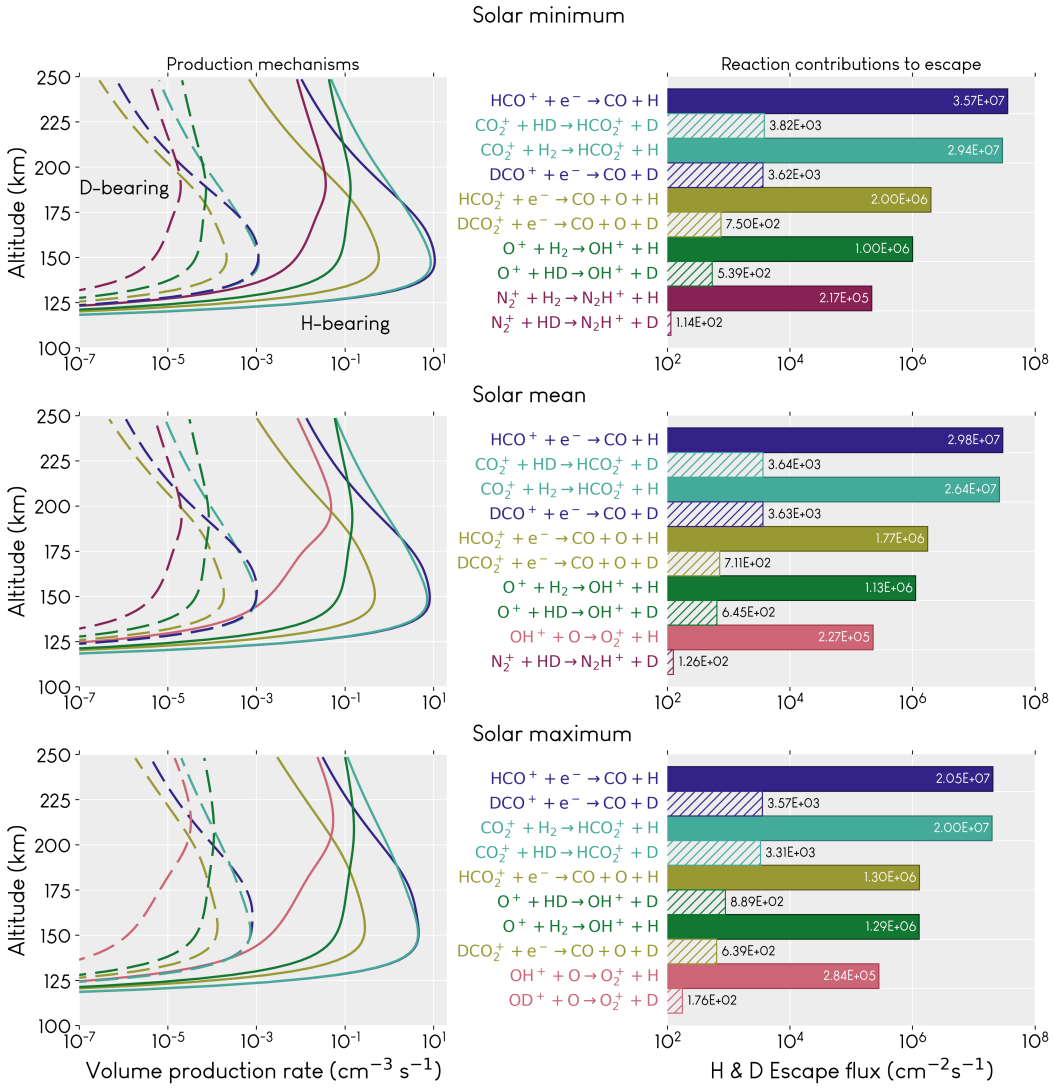

Figure 5. Volume production rates of escaping atoms (panels a, c, e) and integrated escape flux of the produced atomic H or D (b, d, f) for the dominant five chemical pathways producing hot H (solid lines/solid bars) and hot D (dotted lines/dot-fill bars).

per atmosphere and an underprediction of NO^+, but considering we are using a 1D model that does not account for local and short-term variations and we have not made any model changes to match data, we find the output acceptable.

3.2 Are the dominant production mechanisms of hot H and D analogous or dissimilar?

Figure 5 shows the production mechanisms for hot H and D, which are mostly similar.

The most important reaction driving the production of hot D (H) below 200 km in solar mean and maximum is DCO^+(HCO^+) dissociative recombination (DR), with $CO_2{}^+$+ HD (H_2) a close second. HCO^+ DR dominates for hot H under all solar conditions, but for hot D, $CO_2{}^+$+ HD marginally dominates over DCO^+ DR during solar minimum at certain altitudes, making it the dominant source of escaping hot D at solar minimum. This is because the density of HD relative to DCO^+ is larger than H_2 relative to HCO^+.

	Thermal escape ($cm^{-2}s^{-1}$)				Non-thermal escape ($cm^{-2}s^{-1}$)				Total escape ($cm^{-2}s^{-1}$)		
	H	D	H_2	HD	H	D	H_2	HD	H	D	H + D
Solar minimum	1.75×10^8	80	1.6×10^5	0.13	6.5×10^7	9387	15351	19	2.3996×10^8	9467	2.4×10^8
Solar mean	1.833×10^8	309	5.0×10^5	0.89	5.6×10^7	9219	12331	18	2.39966×10^8	9529	2.4×10^8
Solar maximum	1.834×10^8	6740	8.2×10^6	98	4.0×10^7	8908	7669	16	2.39969×10^8	15747	2.4×10^8

Table 2. Amount of thermal and non-thermal escape of atomic and molecular H and D species for the three solar conditions. The total escape amounts to 2.4×10^8 because in the equilibrium atmosphere, the ratio ϕ_H/ϕ_O approaches 2, as O escape is fixed at 1.2 $\times10^8$ (see Section 2.3). Escaping atoms and molecules are sourced from the neutral species; densities for the associated species are shown in Figure S2.

The rates of production from these two processes for hot D are very close; minor changes in conditions, including normal fluctuations in the real atmosphere, could likely change this relationship. Above 200 km, $CO_2{}^+$+ H_2 dominates for hot H production, but high-altitude hot D comes mostly from O^++ HD.

$DCO_2{}^+$($HCO_2{}^+$) DR is the third most important reaction during quiet solar conditions, but it is eclipsed by O+ + HD (H_2) during solar maximum. Under quieter solar conditions, the fifth place position is seized by $N_2{}^+$+ HD (H_2). But as the thermosphere warms, OD (OH) + O claims the fifth place, first for the H species and then for the D species. This appears to be because the dominant reaction involving $OH^+$and $OD^+$is the reaction O^++ H_2 (HD) $\rightarrow$ OH^+(OD^+) + H. This reaction also has a rate coefficient that is independent of temperature, whereas $N_2{}^+$+ HD (H_2) has a rate coefficient which decreases with temperature.

3.3 What is the magnitude of non-thermal escape of D, and under which conditions does it dominate thermal escape?

Figure 6 shows the relative contributions of thermal and non-thermal escape of atomic H and D and thermal escape of the molecular species; the associated escape fluxes to space are given in Table 2. The density profiles of the neutral species, from which the escape is sourced, appear in Figure S2; an upcoming publication will focus on variations in these neutral species and their D/H ratios. As has been asserted in the literature (V. A. Krasnopolsky, 2002), thermal escape is the dominant loss process for atomic H, with non-thermal escape of H making up a gradually reducing share across the solar cycle. The picture looks very different for D, for which 62-99.3% of escape is non-thermal depending on solar conditions. Note that, as shown in Table 2, the total escape of H and D adds to 2.4×10^8 $cm^{-2}s^{-1}$ under all solar conditions due to the boundary conditions (see Section 2.3).

Previous work has predicted that thermal escape of D should actually dominate at solar maximum (V. A. Krasnopolsky, 2002) and that non-thermal escape of D in the form of larger molecules such as HD, OD, and HDO could be up to 15% (Gacesa et al., 2018), whereas our results show that non-thermal escape of HD is so negligible as to not appear at all in Figure 6. Besides the fact that we do not account for excited rotational states of HD, the discrepancy also likely arises from our chosen methods. Our non-thermal escape probability curve is valid for hot atoms with 5 eV of energy, and we do not account at all for branching to excited internal states of the other product; we assume that all atomic H and D produced by exothermic reactions are produced "hot". In reality, not all exothermic heat is dumped directly into the lone atoms all the time. With proper accounting for these intricate branching ratios, our calculated total of non-thermally escaping atomic D would likely decrease. We also do not calculate non-thermal OD escape.

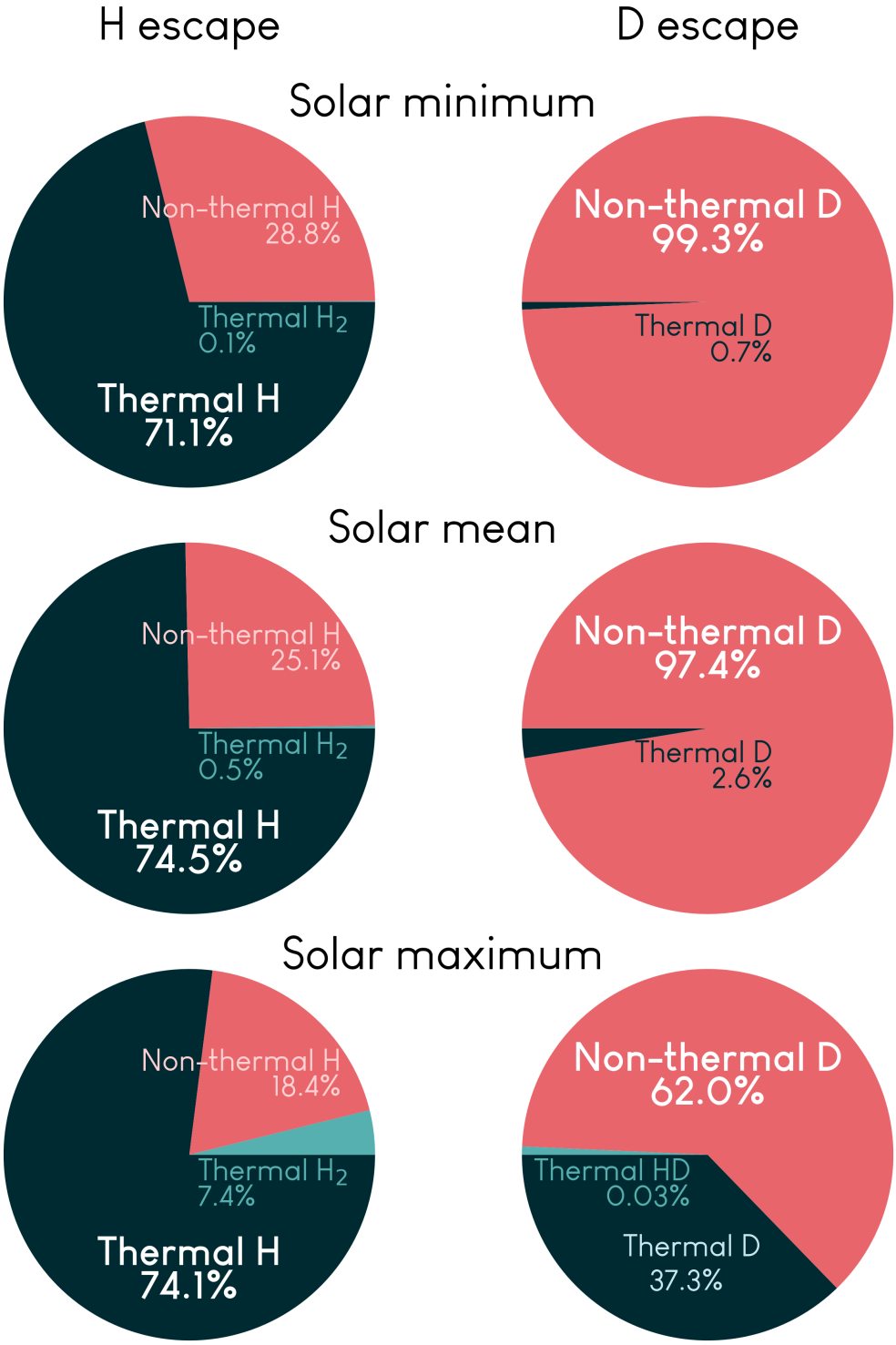

Figure 6. Relative escape contributions for H and D. As expected based on the literature, thermal escape dominates for H during all solar conditions, but non-thermal escape dominates D escape, even at solar maximum. Although we do model non-thermal escape of H_2 and HD, their contributions are completely negligible (see Table 2).

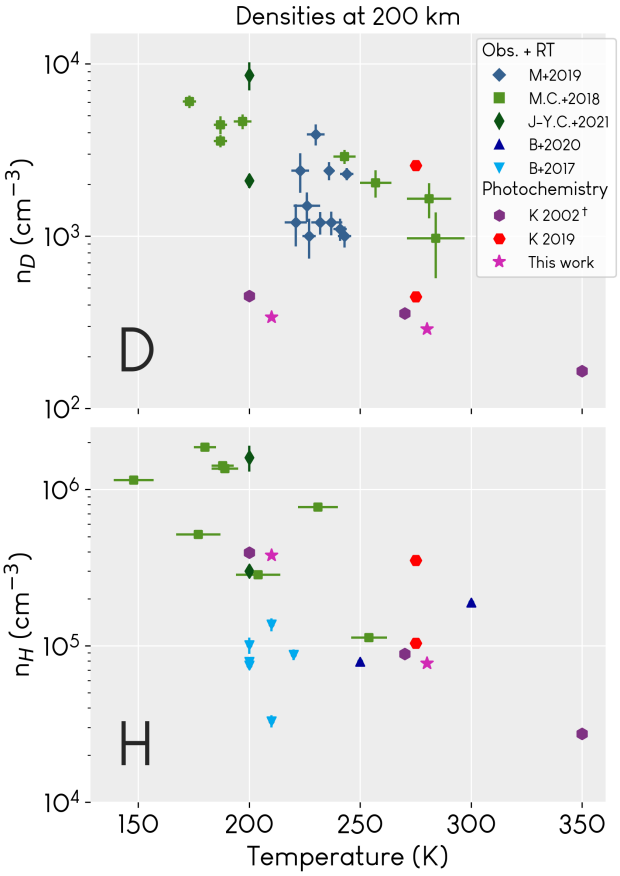

Figure 7. D and H densities at 200 km († 250 km) from multiple studies. Data represent multiple solar zenith angles, seasons, hemispheres, etc. M+2019: Mayyasi et al. (2019). M.C.+2018: Chaffin et al. (2018). J-Y.C.+2021: Chaufray et al. (2021). B+2020, 2017: Bhattacharyya et al. (2020, 2017). K 2002, 2019: V. A. Krasnopolsky (2002, 2019). Entries under "Obs. + RT" used brightness observations from either HST (Bhattacharyya et al., 2017) or MAVEN IUVS (all others) with radiative transfer modeling for density retrievals. For these studies, invisible density error bars indicate uncertainty smaller than the marker size. Temperature error bars indicate that temperature was retrieved from spacecraft data, while missing temperature error bars mean it was a model parameter or output. Uncertainties for photochemistry studies are not calculated. Photochemical modeling typically reports an order of magnitude less D than other methods, which may be due to observation biases toward times of brighter D emission. There is no similar discrepancy in H densities.

4 Discussion

Figure 7 places our D and H densities in context with other studies. We have only consolidated reported densities; we make no attempt to filter by observation geometries. Nevertheless, there appears to be an inverse relationship of densities and temperature for both species. We can also see that photochemical models (red/purple/pink points) produce D densities that are an order of magnitude smaller than densities retrieved using observations and radiative transfer modeling; the same discrepancy does not occur for the H densities. Deuterium Lyman α is difficult to separate from hydrogen Lyman α; the D density discrepancy may potentially be explained by a systematic bias toward anomalously bright D emissions. One exception is the density of D at ∼2500 and T= 275K in the work by V. A. Krasnopolsky (2019); this point represents a model run with a high amount of water in the thermosphere, whereas all the other photochemical results have a comparatively lower water abundance. This comparison demonstrates that our model output is in reasonable agreement with other works.

As mentioned previously, we do not include cloud or dust microphysics, although these processes do have an important effect on the water cycle. These effects are explored in two recent papers using the Laboratoire de Météorologie Dynamique Planetary Climate Model (LMD-PCM) to study the creation of water ice clouds and their role in controlling the D/H ratio (Vals et al., 2022; Rossi et al., 2022).

4.1 Can inclusion of non-thermal escape in the model yield an estimation of water loss similar to the amount calculated in geological studies?

By considering both thermal and non-thermal escape, we can now compute the D/H fractionation factor, which represents the relative efficiency of D and H escape. It is defined as:

$$\mathrm{f} = \frac{\phi_\mathrm{D}/\phi_\mathrm{H}}{[\mathrm{HDO}]_\mathrm{s}/2[\mathrm{H_2O}]_\mathrm{s}} \tag{4}$$

Where $\phi_X = \phi_{X,t} + \phi_{X,n}$ is the rate at which species X (D or H) escapes from the top of the atmosphere due to both thermal (t) and non-thermal (n) processes. The denominator represents the D/H ratio in water measured at the surface (s), which is a proxy for the D/H ratio in the larger exchangeable reservoir.

The fractionation factor is important not only because it tells us how efficient loss of D is compared to loss of H, but also because it is useful for calculating the integrated water loss from a planet. Long-term enrichment of the heavy isotope (D) due to differential escape of D and H can be modeled using Rayleigh fractionation (Chamberlain & Hunten, 1987; Yung & DeMore, 1998):

$$\frac{(\mathrm{D/H})_\mathrm{now}}{(\mathrm{D/H})_\mathrm{past}} = \left(\frac{[\mathrm{H}]_\mathrm{past}}{[\mathrm{H}]_\mathrm{now}}\right)^{1-\mathrm{f}} \tag{5}$$

Equation 5 is used to calculate water loss from Mars. The D/H ratio on the left hand side represents the ratio measured in water in the exchangeable reservoir (the seasonal polar caps, near-surface ices, and atmospheric water vapor), and the ratio $\mathrm{H_2O_{past}/H_2O_{now}}$ can be substituted in on the righthand side and rearranged, obtaining (Cangi et al., 2020) (where W is water):

$$\mathrm{W_{lost}} = \mathrm{W_{now}}\left(\left(\frac{(\mathrm{D/H})_\mathrm{now}}{(\mathrm{D/H})_\mathrm{past}}\right)^{1/(1-\mathrm{f})} - 1\right) \tag{6}$$

Implicit in these equations is the assumption that [H] ≫ [D], so that the past and present abundances of H_2O are reasonable representations of the entire water budget. In the present day, the ratio of D/H is well constrained by many observational studies to be approximately 4-6 × standard mean ocean water (SMOW) (Encrenaz et al., 2018; Villanueva

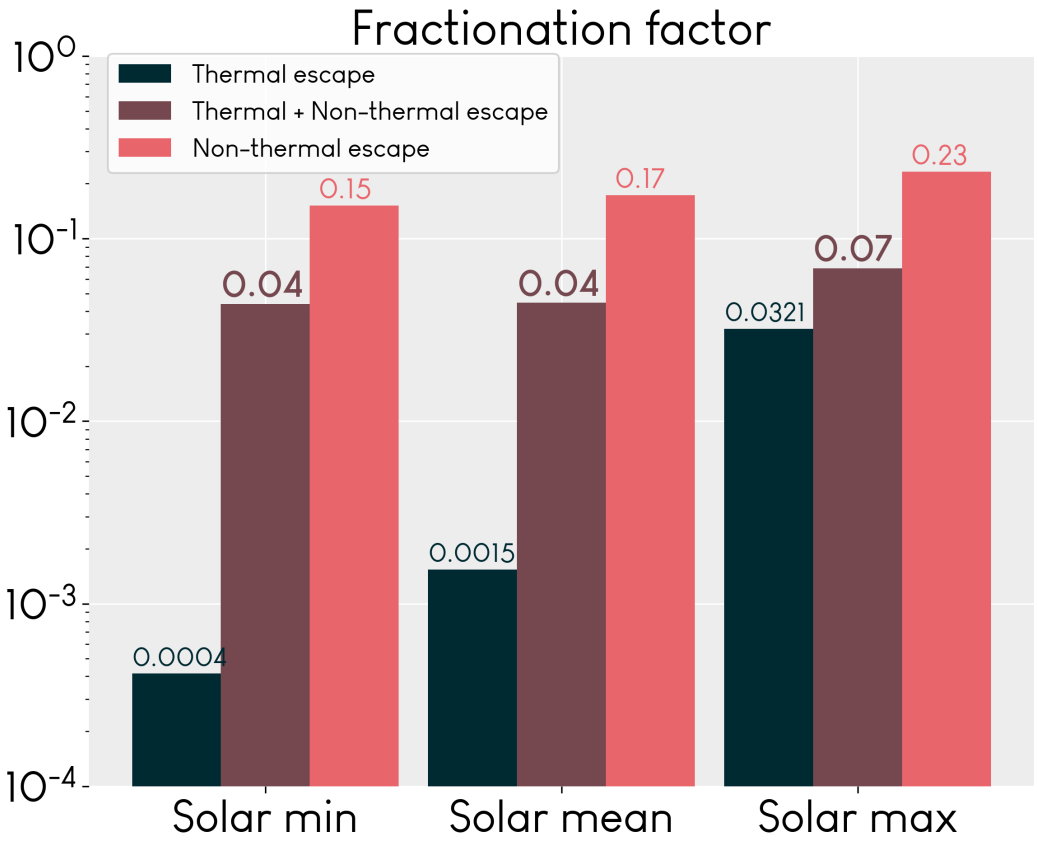

Figure 8. The fractionation factor f for three different modes of escape. Changing solar conditions lead to an orders of magnitude increase in f, as does inclusion of non-thermal escape in the calculation. Fractionation represents the escape efficiency of D compared to H, meaning that $f = 0.04$ represents a 4% escape efficiency of D. Non-thermal escape is an effective escape method for D under all solar conditions.

et al., 2015, and references therein). Current research also has identified a likely present-day exchangeable reservoir water budget of 20-30 m GEL (Lasue et al., 2013, and references therein). By obtaining a reliable value for f, we can combine all these values to calculate the inventory of water on ancient Mars.

Cangi et al. (2020) suggested that the difference between the mean atmospheric f_t (considering only thermal escape) and f_{tn} (considering both thermal and non-thermal escape) was several orders of magnitude. Because they did not directly model non-thermal escape, they arrived at this conclusion by incorporating the non-thermal escape velocity given by V. A. Krasnopolsky et al. (1998) into their model. We are now in a position to compare with those estimates; our calculations of the fractionation factor are shown in Figure 8. Cangi et al. (2020) calculated $f = 0.06$ for their standard atmosphere, based on their modeled thermal escape and estimated non-thermal escape. We calculate a total escape fractionation of $f = 0.04$ for our solar mean atmosphere, which has the same insolation and similar temperatures, and is not far off from their 0.06. Our results are consistent with their thermal escape $f = 0.002$ for the standard atmosphere (roughly equivalent to our solar mean atmosphere). Our results show that while overall D escape at Mars is around 4-7% as efficient as H escape, non-thermal D escape is much more efficient, between 15-23% that of H.

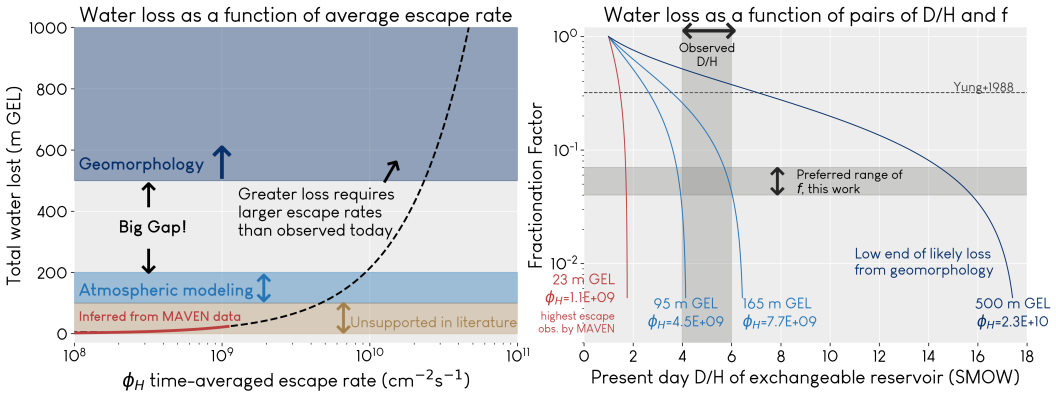

Figure 9. a): Possible water loss as a function of long-term average H escape rate ϕ_H, $W_{lost} = \bar{\phi}_H t$, where t = 4.5 billion years. A significant gap separates the amount of water loss inferred from atmospheric modeling and geomorphological studies. Additionally, escape rates determined from MAVEN data enable very small amounts of water loss that are not consistent with the geological evidence. b): Water loss lines represent solutions to equation 6, assuming 30 m GEL in the present-day exchangeable reservoir. The regions matching the best values of D/H and f are shaded in gray, with the overlapped rectangle representing our best estimate of the present-day atmosphere. (The fractionation factor calculated by Yung et al. (1988) is shown for reference, though it is high due to the highly uncertain exospheric temperatures then used.)

Our results yield integrated water loss of 147–158 m GEL (present day exchangeable reservoir = 30 m GEL, $f = 0.04$–0.07, D/H=5.5×SMOW). This total loss still does not agree with the geological estimates of 500+ m GEL (Lasue et al., 2013). The discrepancy is summarized in Figure 9. Figure 9a shows the gap between the amount of water loss calculated by atmospheric models (Yung et al., 1988; Kass & Yung, 1999; V. Krasnopolsky, 2000; V. A. Krasnopolsky, 2002; Cangi et al., 2020) and that inferred from geomophological observations (Lasue et al., 2013, and references therein). The time-averaged H escape rate curve suggests that the rates observed today (Jakosky et al., 2018) are unlikely to be near the average, and that escape was likely higher in the distant past, enabling greater water loss. Plausible explanations could include periods of hydrodynamic escape, a more EUV-active young sun driving greater photochemistry, extreme obliquities (Wordsworth, 2016; Laskar et al., 2004), or other as of yet unknown dynamics.

It is also possible that some water may have been sequestered into the surface. Recent work by Scheller et al. (2021) suggests that this amount may have accounted for between 30-99% of all missing water. More smaller-scale models and many observations will be needed to constrain this large range further. Hydrated minerals may contain 130-260 m GEL equivalent water Wernicke and Jakosky (2021), but the time of emplacement and any fractionation of the process is unclear. In general, due to the chaotic evolution of obliquity (Laskar et al., 2004) over Mars' history, it is extremely difficult to qualitatively describe escape rates in the past. Although it is difficult to extrapolate much from the present-day rates, high loss of water via escape to space is not ruled out.

Figure 9b also helps demonstrate when it is important to know the value of f rather precisely. Discriminating between $f = 0.04$ or $f = 0.07$ is not particularly important: below $f = 0.1$, water loss curves are relatively vertical, meaning that a change in f does not equate to a significant change in water loss, but this is less true the closer f gets to 1. (For another view, see Figure S4 for water loss as a function of f for a single D/H ratio.)

Considered together, these insights tell us that non-thermal escape processes for D are important to model in order to accurately understand how D escapes from Mars. This conclusion may not hold for other planets, moons, or exoplanets; on bodies which are colder, larger, or otherwise less conducive to thermal escape, non-thermal escape may have a greater role to play.

4.2 Other non-thermal processes

We do not account for the collision of H or D with hot oxygen, which is another significant source of hot atoms in the martian atmosphere. Assuming an exospheric temperature of 240 K, Gacesa et al. (2012) calculated that 1.9×10^5 $cm^{-2}s^{-1}$ H_2 molecules escape as a result of collision with hot oxygen, which is larger than our non-thermal H_2 flux by two orders of magnitude (see Table 2). They also estimate that 74 HD molecules $cm^{-2}s^{-1}$ escape via this mechanism. This would bring our total HD escape to approximately 100 $cm^{-2}s^{-1}$, an order of magnitude larger than our current result. Other species may also play a role; Gacesa et al. (2017) calculate that the total non-thermal escape of OH is 1.07×10^{23} s^{-1}, i.e. 7.4×10^5 $cm^{-2}s^{-1}$. Even added together, these numbers are all still orders of magnitude smaller than the non-thermal atomic escape fluxes, and will not significantly affect our results. If we included them, the net effect would be to boost H escape, decreasing the fractionation factor and total water loss.

Energization of atomic H and D by collision with hot oxygen may be significant. Shematovich (2013) estimates, for specific density profiles and temperatures, a total possible escape flux of hot H produced this way to be 6×10^6 $cm^{-2}s^{-1}$at low solar activity. This begins to approach our non-thermal H escape (see Table 2). Our non-thermal D escape is 3 orders of magnitude lower than the H escape. If we crudely apply this scaling relation to hot O collisions with D, we can expect that this pathway might produce D escape on the order of 10^3, which is the same order as our calculated non-thermal escape fluxes. However, since it is not significantly larger, we can at least expect that the exclusion of hot O collisions with H and D would not significantly change our primary conclusions.

4.3 Future opportunities and directions

There are several things that could enhance our model. The first likely avenue worthy of exploration would be to perform a similar study, but with a more physically-motivated parameterization of atomic O escape. Fixing the O escape at 1.2×10^8 $cm^{-2}s^{-1}$was sufficient for the scope of this work; our results represent long-term equilibrium, when it is possible to adopt reasonable means for parameters like O escape. Adding a dynamically evolving escape flux boundary condition for atomic O would enable a more comprehensive understanding of shorter-term variations in H and D escape rates, such as a result of regular seasonal cycles. This would better capture the interplay between the hydrogen species and CO_2, the main component of the atmosphere and a significant source of O. This would also present an opportunity to include processes more important to O loss, such as ion pickup, ion/polar outflow, and sputtering. We do not include these as we focus on H and D loss, which are dominated by other processes.

We have also been forced to make some unavoidable assumptions about the basic chemistry, owing to a lack of laboratory data. While we have made a best attempt to use existing reaction rate coefficient data from several different papers and databases, a comprehensive catalogue of rate coefficients, branching ratios, and cross sections for deuterated reactions is not available in the literature at this time. Most especially, future photochemical models would benefit from accurate photoabsorption cross sections for deuterated neutrals other than HDO (including OD and HD in particular), and measured reaction rate coefficients for as many of the deuterated reactions with estimated rates in Table 1 as possible. While not all reactions will significantly affect the chemistry, certain rates that dominate production or loss of a species can have strong effects, affecting densities up to a few orders of magnitude (see, for example, Fox et al. (2017)).

Photochemical modeling often entails excluding some important processes that are better captured in higher-dimensional models. Our model is the first to couple the ion and neutral atmospheres from the upper atmosphere down to the surface, but there is still an opportunity for future work to give more attention to surface-atmosphere interactions. Our inclusion of surface-atmosphere interactions is primarily relegated to surface density boundary conditions for certain species. A more detailed parameterization of processes such as volcanic outgassing, major seasonal changes in the polar caps, water adsorption and desorption on dust grains and dust lifting, deposition of volatiles, and the role of non-volatiles such as perchlorates, salts, and other non-water ices could yield new insights into the planetary climate system as a whole.

Our results also have implications for the detectability of deuterated ions by present and future Mars missions. Using MAVEN's NGIMS instrument, the deuterated ions that we model typically occupy the same mass/charge ratio bin as a more prevalent H-bearing species. For example, D^+occupies the same bin as $H_2{}^+$, but the latter is far more abundant. The deuterated species in our model which do not overlap with an H-bearing species are H_2D^+(mass bin 4), $HD_2{}^+$(5), H_2DO^+(20), $HDO_2{}^+$(35), and ArD^+(42). However, several of these species are expected to be very rarefied and thus difficult to detect, and others may overlap with species we do not model that do exist on Mars, such as helium in mass bin 4. These degeneracies make obtaining deuterated ion densities challenging; doing so will require inventive methods applied to existing data or new methods with new instruments.

5 Conclusions

We have used a 1D photochemical model that fully couples ions and neutrals from surface to space to study production of hot D from planetary ionospheric processes. We show that the deuterated ionosphere behaves relatively similar to the H-bearing ionosphere. This result is somewhat expected, as measurements of rate coefficients for deuterated reactions are much less available than the H-bearing counterpart reaction rate coefficients.

For the first time, we have self-consistently quantified, in raw flux and in percent of total escape, the thermal and non-thermal escape fluxes of H and D in both the atomic and molecular forms in equilibrium atmospheres under different solar conditions, and the dominant chemical reactions responsible for producing hot D. Our results confirm earlier suggestions that non-thermal escape dominates D escape at Mars, although our results have shown that this is true throughout the solar cycle rather than just during quiet solar conditions.

We also confirm an earlier prediction (Cangi et al., 2020) that including non-thermal escape when calculating the D/H fractionation factor will result in a fractionation factor several orders of magnitude higher than if it is neglected. However, the resulting fractionation factor is 0.04–0.07, meaning that D escape is only about 4-7% as efficient as H escape. If the fractionation has consistently been this small, and we also assume that the escape rate of H ϕ_H has been similar to the value today through time, it is difficult to ascribe the large amount of water loss that we see indicated in the rock record to atmospheric escape alone. On the other hand, the dust storm season on Mars, as well as normal seasonal variations between perihelion and aphelion, are characterized by spatially and temporally localized enhancements of the D/H ratio, water abundance, and H escape (Villanueva et al., 2021; Daerden et al., 2022; A. Fedorova et al., 2021; Chaffin et al., 2021; Holmes et al., 2021; A. A. Fedorova et al., 2020; Stone et al., 2020; Aoki et al., 2019; Vandaele et al., 2019; Heavens et al., 2018; Chaffin et al., 2017, and references therein). It is not yet clear if enhanced D escape or a heightened fractionation factor also occur along with these seasonal changes, although it seems likely (Alday et al., 2021); if they do, then the assumption of a constant fractionation factor over time cannot hold, and we will have to introduce some additional nuance to our use of Rayleigh fractionation to estimate water loss.

Ongoing improvements in modeling, especially coupling between 1D and 3D models, as well as continual advancements in instrumentation for planetary missions will be necessary to continue putting together the puzzle of water on Mars throughout history.

6 Open Research Statement

The photochemical model used for this work is written for and compatible with Julia 1.7.1 (Bezanson et al., 2017). The model itself, in version 1.0 as used in this work, is available at Zenodo (Cangi & Chaffin, 2022).

A typical use-case of the model is to modify simulation parameters within `PARAMETERS.jl` and to then call `julia converge_new_file.jl` at the command line.

Acknowledgments

This work was supported by three separate funding sources. First, this work was supported by Mars Data Analysis Program grant #NNX14AM20G. Second, this material is based upon work supported by the National Science Foundation Graduate Research Fellowship Program under Grant No. DGE 1650115. Any opinions, findings, and conclusions or recommendations expressed in this material are those of the author(s) and do not necessarily reflect the views of the National Science Foundation. Third, this work was supported by NASA's FINESST Program (Grant #80NSSC22K1326).

References

Alday, J., Trokhimovskiy, A., Irwin, P. G. J., Wilson, C. F., Montmessin, F., Lefèvre, F., ... Shakun, A. (2021, June). Isotopic fractionation of water and its photolytic products in the atmosphere of Mars. *Nature Astronomy*, *5*, 943-950. doi: 10.1038/s41550-021-01389-x

Alsaeed, N. R., & Jakosky, B. M. (2019). Mars Water and D/H Evolution From 3.3 Ga to Present. *Journal of Geophysical Research: Planets*, *124*. doi: 10.1029/2019JE006066

Anicich, V. G. (2003). *An index of the literature for bimolecular gas phase cation-molecule reaction kinetics* (JPL Publication No. 03-19). Pasadena: Jet Propulsion Laboratory.

Aoki, S., Vandaele, A. C., Daerden, F., Villanueva, G. L., Liuzzi, G., Thomas, I. R., ... Lopez-Moreno, J. J. (2019, December). Water Vapor Vertical Profiles on Mars in Dust Storms Observed by TGO/NOMAD. *Journal of Geophysical Research (Planets)*, *124*(12), 3482-3497. doi: 10.1029/2019JE006109

Banaszkiewicz, M., Lara, L. M., Rodrigo, R., López-Moreno, J. J., & Molina-Cuberos, G. J. (2000, October). A Coupled Model of Titan's Atmosphere and Ionosphere. *Icarus*, *147*(2), 386-404. doi: 10.1006/icar.2000.6448

Bauer, S. J. (1973). Chemical processes. In *Physics of planetary ionospheres* (pp. 82–95). Springer.

Benna, M., Mahaffy, P. R., Grebowsky, J. M., Fox, J. L., Yelle, R. V., & Jakosky, B. M. (2015, November). First measurements of composition and dynamics of the Martian ionosphere by MAVEN's Neutral Gas and Ion Mass Spectrometer. *Geophysical Research Letters*, *42*(21), 8958-8965. doi: 10.1002/2015GL066146

Bezanson, J., Edelman, A., Karpinski, S., & Shah, V. B. (2017). Julia: A fresh approach to numerical computing. *SIAM review*, *59*(1), 65–98.

Bhattacharyya, D., Chaufray, J. Y., Mayyasi, M., Clarke, J. T., Stone, S., Yelle, R. V., ... Schneider, N. M. (2020). Two-dimensional model for the martian exosphere: Applications to hydrogen and deuterium Lyman α observations. *Icarus*, *339*, 113573. doi: 10.1016/j.icarus.2019.113573

Bhattacharyya, D., Clarke, J. T., Chaufray, J. Y., Mayyasi, M., Bertaux, J. L., Chaffin, M. S., ... Villanueva, G. L. (2017). Seasonal Changes in Hydrogen Escape From Mars Through Analysis of HST Observations of the Martian

Exosphere Near Perihelion. *Journal of Geophysical Research (Space Physics)*, *122*(11), 11,756-11,764. doi: 10.1002/2017JA024572

Burkholder, J., Sander, S., Abbatt, J., Barker, J., Cappa, C., Crounse, J., ... Wine, P. H. (2019). *Chemical kinetics and photochemical data for use in atmospheric studies, evaluation no. 19* (JPL Publication No. 19-5). Pasadena: Jet Propulsion Laboratory.

Cangi, E. M., & Chaffin, M. (2022, December). *emcangi/dh_ions: Jump v1.0.* Zenodo. Retrieved from `https://doi.org/10.5281/zenodo.7392379` doi: 10.5281/zenodo.7392379

Cangi, E. M., Chaffin, M. S., & Deighan, J. (2020). Higher Martian Atmospheric Temperatures at All Altitudes Increase the D/H Fractionation Factor and Water Loss. *Journal of Geophysical Research: Planets*, *125*(12), 1–15. doi: 10.1029/2020JE006626

Cazaux, S., Cobut, V., Marseille, M., Spaans, M., & Caselli, P. (2010, November). Water formation on bare grains: When the chemistry on dust impacts interstellar gas. *Astronomy & Astrophysics*, *522*, A74. doi: 10.1051/0004-6361/201014026

Chaffin, M. S., Chaufray, J. Y., Deighan, J., Schneider, N. M., Mayyasi, M., Clarke, J. T., ... Jakosky, B. M. (2018, August). Mars H Escape Rates Derived From MAVEN/IUVS Lyman Alpha Brightness Measurements and Their Dependence on Model Assumptions. *Journal of Geophysical Research (Planets)*, *123*(8), 2192-2210. doi: 10.1029/2018JE005574

Chaffin, M. S., Deighan, J., Schneider, N. M., & Stewart, A. I. F. (2017, January). Elevated atmospheric escape of atomic hydrogen from Mars induced by high-altitude water. *Nature Geoscience*, *10*(3), 174-178. doi: 10.1038/ngeo2887

Chaffin, M. S., Kass, D. M., Aoki, S., Fedorova, A. A., Deighan, J., Connour, K., ... Korablev, O. I. (2021, August). Martian water loss to space enhanced by regional dust storms. *Nature Astronomy*, *5*, 1036-1042. doi: 10.1038/s41550-021-01425-w

Chamberlain, J. W., & Hunten, D. M. (1987). *Theory of planetary atmospheres. An introduction to their physics andchemistry.* (Vol. 36).

Chaufray, J. Y., Mayyasi, M., Chaffin, M., Deighan, J., Bhattacharyya, D., Clarke, J., ... Jakosky, B. (2021, April). Estimate of the D/H Ratio in the Martian Upper Atmosphere from the Low Spectral Resolution Mode of MAVEN/IUVS. *Journal of Geophysical Research (Planets)*, *126*(4), e06814. doi: 10.1029/2020JE006814

Cheng, B.-M., Chew, E. P., Liu, C.-P., Bahou, M., Lee, Y.-P., Yung, Y. L., & Gerstell, M. F. (1999, December). Photo-induced fractionation of water isotopomers in the Martian atmosphere. Geophys. Res. Lett., *26*(24), 3657-3660. doi: 10.1029/1999GL008367

Cheng, B. M., Chung, C. Y., Bahou, M., Lee, Y. P., Lee, L. C., Van Harrevelt, R., & Van Hemert, M. C. (2004). Quantitative spectroscopic and theoretical study of the optical absorption spectra of H_2O, HOD, and D_2O in the 125-145 nm region. *Journal of Chemical Physics*, *120*. doi: 10.1063/1.1630304

Daerden, F., Neary, L., Villanueva, G., Liuzzi, G., Aoki, S., Clancy, R. T., ... Vandaele, A. C. (2022, February). Explaining NOMAD D/H Observations by Cloud-Induced Fractionation of Water Vapor on Mars. *Journal of Geophysical Research (Planets)*, *127*(2), e07079. doi: 10.1029/2021JE007079

Dobrijevic, M., Loison, J. C., Hickson, K. M., & Gronoff, G. (2016, April). 1D-coupled photochemical model of neutrals, cations and anions in the atmosphere of Titan. *Icarus*, *268*, 313-339. doi: 10.1016/j.icarus.2015.12.045

Encrenaz, T., DeWitt, C., Richter, M. J., Greathouse, T. K., Fouchet, T., Montmessin, F., ... Sagawa, H. (2018, April). New measurements of D/H on Mars using EXES aboard SOFIA. *Astronomy & Astrophysics*, *612*, A112. doi: 10.1051/0004-6361/201732367

Ergun, R. E., Morooka, M. W., Andersson, L. A., Fowler, C. M., Delory, G. T., Andrews, D. J., ... Jakosky, B. M. (2015, November). Dayside electron temperature and density profiles at Mars: First results from the MAVEN Langmuir probe and waves instrument. *Geophysical Research Letters*, *42*(21), 8846-8853. doi: 10.1002/2015GL065280

Fedorova, A., Montmessin, F., Korablev, O., Lefèvre, F., Trokhimovskiy, A., & Bertaux, J.-L. (2021, January). Multi-Annual Monitoring of the Water Vapor Vertical Distribution on Mars by SPICAM on Mars Express. *Journal of Geophysical Research (Planets)*, *126*(1), e06616. doi: 10.1029/2020JE006616

Fedorova, A. A., Montmessin, F., Korablev, O., Luginin, M., Trokhimovskiy, A., Belyaev, D. A., ... Wilson, C. F. (2020, January). Stormy water on Mars: The distribution and saturation of atmospheric water during the dusty season. *Science*, *367*(6475), 297-300. doi: 10.1126/science.aay9522

Fox, J. L. (2015, May). The chemistry of protonated species in the martian ionosphere. *Icarus*, *252*, 366-392. doi: 10.1016/j.icarus.2015.01.010

Fox, J. L., Benna, M., Mahaffy, P. R., & Jakosky, B. M. (2015, November). Water and water ions in the Martian thermosphere/ionosphere. *Geophysical Research Letters*, *42*(21), 8977-8985. doi: 10.1002/2015GL065465

Fox, J. L., Benna, M., McFadden, J. P., Jakosky, B. M., & Maven Ngims Team. (2021, April). Rate coefficients for the reactions of $CO_2{}^+$ with O: Lessons from MAVEN at Mars. *Icarus*, *358*, 114186. doi: 10.1016/j.icarus.2020.114186

Fox, J. L., Johnson, A. S., Ard, S. G., Shuman, N. S., & Viggiano, A. A. (2017, August). Photochemical determination of O densities in the Martian thermosphere: Effect of a revised rate coefficient. *Geophysical Research Letters*, *44*(16), 8099-8106. doi: 10.1002/2017GL074562

Gacesa, M., Lewkow, N., & Kharchenko, V. (2017). Non-thermal production and escape of oh from the upper atmosphere of mars. *Icarus*, *284*, 90–96.

Gacesa, M., Lillis, R., Deighan, J., Elrod, M., Fox, J. L., & the MAVEN NGIMS team. (2018). Non-thermal escape rates of light species from mars using maven in-situ measurements. In *European planetary science congress* (pp. EPSC2018–604).

Gacesa, M., Zhang, P., & Kharchenko, V. (2012, May). Non-thermal escape of molecular hydrogen from Mars. *Geophysical Research Letters*, *39*(10), L10203. doi: 10.1029/2012GL050904

Geppert, W. D., Thomas, R. D., Ehlerding, A., Hellberg, F., Österdahl, F., Hamberg, M., ... Larsson, M. (2005, January). Dissociative recombination branching ratios and their influence on interstellar clouds. In *Journal of physics conference series* (Vol. 4, p. 26-31). doi: 10.1088/1742-6596/4/1/004

Gregory, B. S., Elliott, R. D., Deighan, J., Gröller, H., & Chaffin, M. S. (2022). HCO+ dissociative recombination: A significant driver of nonthermal hydrogen loss at Mars. *Journal of Geophysical Research: Planets*, *(to be submitted)*.

Halekas, J. S., Brain, D. A., Luhmann, J. G., DiBraccio, G. A., Ruhunusiri, S., Harada, Y., ... Jakosky, B. M. (2017, November). Flows, Fields, and Forces in the Mars-Solar Wind Interaction. *Journal of Geophysical Research (Space Physics)*, *122*(11), 11,320-11,341. doi: 10.1002/2017JA024772

Hanley, K. G., Fowler, C. M., McFadden, J. P., Mitchell, D. L., & Curry, S. (2022, September). MAVEN-STATIC Observations of Ion Temperature and Initial Ion Acceleration in the Martian Ionosphere. Geophys. Res. Lett., *49*(18). doi: 10.1029/2022GL100182

Heavens, N. G., Kleinböhl, A., Chaffin, M. S., Halekas, J. S., Kass, D. M., Hayne, P. O., ... Schofield, J. T. (2018). Hydrogen escape from Mars enhanced by deep convection in dust storms. *Nature Astronomy*, *2*. doi: 10.1038/s41550-017-0353-4

Holmes, J. A., Lewis, S. R., Patel, M. R., Chaffin, M. S., Cangi, E. M., Deighan, J., ... Vandaele, A. C. (2021, October). Enhanced water loss from the

730 martian atmosphere during a regional-scale dust storm and implications for
731 long-term water loss. *Earth and Planetary Science Letters*, *571*, 117109. doi:
732 10.1016/j.epsl.2021.117109
733 Jakosky, B. M., Brain, D., Chaffin, M., Curry, S., Deighan, J., Grebowsky, J., ...
734 Zurek, R. (2018, November). Loss of the Martian atmosphere to space:
735 Present-day loss rates determined from MAVEN observations and integrated
736 loss through time. *Icarus*, *315*, 146-157. doi: 10.1016/j.icarus.2018.05.030
737 Kass, D. M., & Yung, Y. L. (1999, January). Water on Mars: Isotopic constraints on
738 exchange between the atmosphere and surface. *Geophysical Research Letters*,
739 *26*(24), 3653-3656. doi: 10.1029/1999GL008372
740 Korolov, I., Plasil, R., Kotrik, T., Dohnal, P., & Glosik, J. (2009, February). Re-
741 combination of HCO+ and DCO+ ions with electrons. *International Journal*
742 *of Mass Spectrometry*, *280*(1-3), 144-148. doi: 10.1016/j.ijms.2008.07.023
743 Krasnopolsky, V. (2000, December). NOTE: On the Deuterium Abundance on Mars
744 and Some Related Problems. *Icarus*, *148*(2), 597-602. doi: 10.1006/icar.2000
745 .6534
746 Krasnopolsky, V. A. (2002, December). Mars' upper atmosphere and iono-
747 sphere at low, medium, and high solar activities: Implications for evolution
748 of water. *Journal of Geophysical Research (Planets)*, *107*(E12), 5128. doi:
749 10.1029/2001JE001809
750 Krasnopolsky, V. A. (2019, March). Photochemistry of water in the martian ther-
751 mosphere and its effect on hydrogen escape. *Icarus*, *321*, 62-70. doi: 10.1016/
752 j.icarus.2018.10.033
753 Krasnopolsky, V. A., Mumma, M. J., & Randall Gladstone, G. (1998, June). De-
754 tection of Atomic Deuterium in the Upper Atmosphere of Mars. *Science*, *280*,
755 1576. doi: 10.1126/science.280.5369.1576
756 Lammer, H., Kolb, C., Penz, T., Amerstorfer, U. V., Biernat, H. K., & Bodiselitsch,
757 B. (2003). Estimation of the past and present Martian water-ice reservoirs
758 by isotopic constraints on exchange between the atmosphere and the surface.
759 *International Journal of Astrobiology*, *2*. doi: 10.1017/S1473550403001605
760 Laskar, J., Correia, A., Gastineau, M., Joutel, F., Levrard, B., & Robutel, P. (2004).
761 Long term evolution and chaotic diffusion of the insolation quantities of Mars.
762 *Icarus*, *170*. doi: 10.1016/J.ICARUS.2004.04.005
763 Lasue, J., Mangold, N., Hauber, E., Clifford, S., Feldman, W., Gasnault, O., ...
764 Mousis, O. (2013). Quantitative Assessments of the Martian Hydrosphere.
765 *Space Science Reviews*, *174*. doi: 10.1007/s11214-012-9946-5
766 Manion, J. A., Huie, R. E., Levin, R. D., Burgess Jr., D. R., Orkin, V. L., Tsang,
767 W., ... Frizzell, D. H. (2015). *NIST Chemical Kinetics Database.* Retrieved
768 2015-09, from `http://kinetics.nist.gov/`
769 Matta, M., Withers, P., & Mendillo, M. (2013, May). The composition of Mars' top-
770 side ionosphere: Effects of hydrogen. *Journal of Geophysical Research (Space*
771 *Physics)*, *118*(5), 2681-2693. doi: 10.1002/jgra.50104
772 Mayyasi, M., Bhattacharyya, D., Clarke, J., Catalano, A., Benna, M., Mahaffy, P.,
773 ... Jakosky, B. (2018, September). Significant Space Weather Impact on
774 the Escape of Hydrogen From Mars. *Geophysical Research Letters*, *45*(17),
775 8844-8852. doi: 10.1029/2018GL077727
776 Mayyasi, M., Clarke, J., Bhattacharyya, D., Chaufray, J. Y., Benna, M., Mahaffy,
777 P., ... Jakosky, B. (2019, March). Seasonal Variability of Deuterium in the
778 Upper Atmosphere of Mars. *Journal of Geophysical Research (Space Physics)*,
779 *124*(3), 2152-2164. doi: 10.1029/2018JA026244
780 Millour, E., & Forget, F. (2018). *Mars Climate Database.* Retrieved from `http://`
781 `www-mars.lmd.jussieu.fr/`
782 Molina-Cuberos, G. J., Lichtenegger, H., Schwingenschuh, K., López-Moreno, J. J.,
783 & Rodrigo, R. (2002, May). Ion-neutral chemistry model of the lower iono-
784 sphere of Mars. *Journal of Geophysical Research (Planets)*, *107*(E5), 5027. doi:

10.1029/2000JE001447

Nee, J. B., & Lee, L. C. (1984). Photoabsorption cross section of OD at 115-180 nm. *The Journal of Chemical Physics*, *81*. doi: 10.1063/1.448183

Owen, T., Maillard, J. P., de Bergh, C., & Lutz, B. L. (1988, June). Deuterium on Mars: The Abundance of HDO and the Value of D/H. *Science*, *240*(4860), 1767-1770. doi: 10.1126/science.240.4860.1767

Rahmati, A., Larson, D. E., Cravens, T. E., Lillis, R. J., Halekas, J. S., McFadden, J. P., ... Jakosky, B. M. (2018, May). Seasonal Variability of Neutral Escape from Mars as Derived From MAVEN Pickup Ion Observations. *Journal of Geophysical Research (Planets)*, *123*(5), 1192-1202. doi: 10.1029/2018JE005560

Rossi, L., Vals, M., Alday, J., Montmessin, F., Fedorova, A., Trokhimovskiy, A., ... Millour, E. (2022, August). The HDO Cycle on Mars: Comparison of ACS Observations With GCM Simulations. *Journal of Geophysical Research (Planets)*, *127*(8), e07201. doi: 10.1029/2022JE007201

Sander, S. P., Abbatt, J., Barker, J. R., Burkholder, J. B., Friedl, R. R., Golden, D. M., ... Wine, P. H. (2011). *Chemical Kinetics and Photochemical Data for Use in Atmospheric Studies Evaluation No. 17* (JPL Publication No. 10-6). Pasadena: Jet Propulsion Laboratory. (http://jpldataeval.jpl.nasa.gov)

Scheller, E. L., Ehlmann, B. L., Hu, R., Adams, D. J., & Yung, Y. L. (2021, April). Long-term drying of Mars by sequestration of ocean-scale volumes of water in the crust. *Science*, *372*(6537), 56-62. doi: 10.1126/science.abc7717

Schunk, R., & Nagy, A. (2009). *Ionospheres: Physics, Plasma Physics, and Chemistry*. doi: 10.1017/CBO9780511635342

Shematovich, V. I. (2013, November). Suprathermal oxygen and hydrogen atoms in the upper Martian atmosphere. *Solar System Research*, *47*(6), 437-445. doi: 10.1134/S0038094613060087

Smith, M. D. (2004). Interannual variability in TES atmospheric observations of Mars during 1999-2003. *Icarus*, *167*. doi: 10.1016/j.icarus.2003.09.010

Stone, S. W., Yelle, R. V., Benna, M., Lo, D. Y., Elrod, M. K., & Mahaffy, P. R. (2020, November). Hydrogen escape from Mars is driven by seasonal and dust storm transport of water. *Science*, *370*(6518), 824-831. doi: 10.1126/science.aba5229

Vals, M., Rossi, L., Montmessin, F., Lefèvre, F., Gonzalez-Galindo, F., Fedorova, A., ... Montabone, L. (2022, August). Improved Modeling of Mars' HDO Cycle Using a Mars' Global Climate Model. *Journal of Geophysical Research (Planets)*, *127*(8), e07192. doi: 10.1029/2022JE007192

Vandaele, A. C., Korablev, O., Daerden, F., Aoki, S., Thomas, I. R., Altieri, F., ... Smith, M. D. e. a. (2019). Martian dust storm impact on atmospheric H 2 O and D/H observed by ExoMars Trace Gas Orbiter. *Nature*, *568*. doi: 10.1038/s41586-019-1097-3

Villanueva, G. L., Liuzzi, G., Crismani, M. M. J., Aoki, S., Vandaele, A. C., Daerden, F., ... Lopez-Moreno, J. J. (2021, February). Water heavily fractionated as it ascends on Mars as revealed by ExoMars/NOMAD. *Science Advances*, *7*(7), eabc8843. doi: 10.1126/sciadv.abc8843

Villanueva, G. L., Mumma, M. J., Novak, R. E., Käufl, H. U., Hartogh, P., Encrenaz, T., ... Smith, M. D. (2015, April). Strong water isotopic anomalies in the martian atmosphere: Probing current and ancient reservoirs. *Science*, *348*(6231), 218-221. doi: 10.1126/science.aaa3630

Vuitton, V., Yelle, R. V., Klippenstein, S. J., Hörst, S. M., & Lavvas, P. (2019). Simulating the density of organic species in the atmosphere of Titan with a coupled ion-neutral photochemical model. *Icarus*, *324*, 120–197. Retrieved from `https://doi.org/10.1016/j.icarus.2018.06.013` (Publisher: Elsevier Inc.) doi: 10.1016/j.icarus.2018.06.013

Wakelam, V., & Gratier, P. (2019). *Kinetic Database for Astrochemistry.* Retrieved from `http://kida.obs.u-bordeaux1.fr/contact.html`

Wernicke, L. J., & Jakosky, B. M. (2021, March). Martian Hydrated Minerals: A Significant Water Sink. *Journal of Geophysical Research (Planets)*, *126*(3), e06351. doi: 10.1029/2019JE006351

Woods, T. N., Chamberlin, P. C., Harder, J. W., Hock, R. A., Snow, M., Eparvier, F. G., ... Richard, E. C. (2019). *LISIRD (LASP Interactive Solar Irradiance Datacenter).* Retrieved from `http://lasp.colorado.edu/lisird/`

Wordsworth, R. (2016). The Climate of Early Mars. *Annual Review of Earth and Planetary Sciences*, *44*. doi: 10.1146/annurev-earth-060115-012355

Yung, Y. L., & DeMore, W. B. (1998). *Photochemistry of Planetary Atmospheres.* Oxford University Press.

Yung, Y. L., Wen, J.-S., Moses, J. I., Landry, B. M., Allen, M., & Hsu, K.-J. (1989). Hydrogen and deuterium loss from the terrestrial atmosphere: A quantitative assessment of nonthermal escape fluxes. *Journal of Geophysical Research*, *94*.

Yung, Y. L., Wen, J.-S., Pinto, J. P., Allen, M., Pierce, K. K., & Paulson, S. (1988, October). HDO in the Martian atmosphere: Implications for the abundance of crustal water. *Icarus*, *76*(1), 146-159. doi: 10.1016/0019-1035(88)90147-9

Zahnle, K., Haberle, R. M., Catling, D. C., & Kasting, J. F. (2008). Photochemical instability of the ancient Martian atmosphere. *Journal of Geophysical Research E: Planets*, *113*. doi: 10.1029/2008JE003160